nature communications

Article

https://doi.org/10.1038/s41467-025-62083-4

# A legume cellulase required for rhizobial infection and colonization in root nodule symbiosis

Received: 19 October 2024

Accepted: 3 July 2025

Published online: 19 July 2025

Check for updates

Li Zhao[1,3], Chuan-Ya Ji[1,3], Jeremy D. Murray[2] & Cheng-Wu Liu[1]

In root nodule symbiosis, the accommodation of rhizobia in legumes necessitates extensive plant cell wall remodeling to build infection threads (ITs) for rhizobia travelling into nodules, and to subsequently release rhizobia from ITs to form nitrogen fixing symbiosomes. The molecular and cellular mechanisms underlying these processes are obscure. Here we report that *Medicago truncatula Glycoside Hydrolase 9C2* (*GH9C2*) is required for both rhizobial infection and nodule colonization. The *gh9c2–1* mutant exhibits incompetent nodules with disorganized ITs and defective rhizobial release, likely due to cellulose accumulation. GH9C2 localizes to IT wall and rhizobial release sites, and cellulase activity is indispensable for GH9C2 function. CBM49 domain of GH9C2 is required for rhizobial infection but not for rhizobial release. Furthermore, *GH9C1*and *NPL* act synergistically with *GH9C2* in rhizobial infection. Our finding reveals transient IT-derived structures, the rhizobial release foci and uncovers a mechanism mediated by host cellulases for the symbiotic colonization by rhizobia.

The legume-rhizobial symbiosis has great potential for sustainable agriculture, through the provision of fixed nitrogen to the host by rhizobia residing in root nodules[1–3]. The rhizobial nitrogenase catalyzes the conversion of $N_2$ to ammonia, which is made possible by the micro-environment provided by legume host nodule cells[4–7]. However, as soil bacteria, rhizobia first need enter into legume roots, and eventually be taken up in the nodule cells to fix nitrogen, a process known as rhizobial infection[8–11]. Rhizobia enter roots either from between cells (intercellular/"crack entry") or through special intracellular structures called infection threads (ITs), and the latter mode is favored in most legumes, including model legumes such as *Medicago truncatula* and *Lotus japonicus*[12].

Intracellular rhizobial infection starts from rhizobia attachment to root hairs after reciprocal signal exchanges between the two symbiotic partners[13,14], followed by root hair curling with rhizobia entrapped, and the subsequent development of an infection chamber (IC) containing a population of propagating rhizobia known as microcolony[15,16]. A tubular infection thread (IT) then initiates from the IC as a result of inward growth of host cell wall and membrane. As the key structure for intracellular infection, the IT develops down through the root hair, proceeded by the nucleus, which remains connected to the growing IT tip, by an ER-rich cytoplasmic bridge, with rhizobia dividing and moving inside[10,17]. A similar process reiterates in sub-epidermal cell layers, resulting in IT ramification into the cells of developing nodules, ending with release of rhizobia from ITs into mature nodule cells. The final step of this process involves formation of un-walled 'infection droplets', from which rhizobia are released and wrapped by host membrane forming so called 'symbiosomes' where biological nitrogen fixation takes place[18,19].

The plant cell wall plays a key role in plant morphogenesis and development, provides structural support and actively engages in signaling processes in response to biotic and abiotic stresses[20–25]. Growing cells are surrounded by primary cell walls and some differentiated cells also have secondary cell walls[26,27]. The biological function of the plant cell wall depends on its composition, which consists

[1]Ministry of Education Key Laboratory for Cellular Dynamics, School of Life Sciences, Division of Life Sciences and Medicine, University of Science and Technology of China, Hefei, China. [2]National Key Laboratory of Plant Molecular Genetics, CAS-JIC Centre of Excellence for Plant and Microbial Science (CEPAMS), Center for Excellence in Molecular Plant Sciences, Chinese Academy of Sciences, Shanghai, China. [3]These authors contributed equally: Li Zhao, Chuan-Ya Ji. e-mail: cwliu01@ustc.edu.cn

polysaccharide polymers, cell wall proteins and/or phenolic compounds such as lignin and varies in different tissues and plant taxa[28,29]. In eudicots, polysaccharide polymers in the primary cell wall include cellulose, hemicellulose and pectin[20,23]. Cellulose is formed by multiple β−1,4-linked glucan chains and these chains are hydrogen bonded together forming cellulose microfibrils, which is the major load-bearing component of the wall[30–32]. In plant-microbe interactions, pathogens need overcome the plant cell wall barrier, e.g. cellulose microfibrils, by usually loosening or degrading it for the establishment of infection and disease[33–35]. To this end many pathogens secrete an array of cell wall degrading enzymes such as glycosyl hydrolases, or glycoside hydrolases (GH), which cut glycosidic bonds in cell wall polysaccharides[33,36]. Among the GHs, members of GH family 9 (GH9) are endo-β−1,4 glucanases, also known as EGases, or cellulases (EC 3.2.1.4), which are also found in plants and are subdivided into 3 groups, i.e. GH9A, GH9B and GH9C[37–40]. All plant GH9 proteins contain a glycoside hydrolase catalytic domain (CD), while GH9Cs harbor an additional carbohydrate binding domain, CBM49, which was shown to bind cellulose[38]. Although some plant GH9C cellulases have been shown to degrade cellulose and hemicellulose in vitro, in general their function in plant development or plant-microbe interactions are almost unknown[41,42].

Plant cell walls function as important “symbiotic interface” for molecular exchange in plant-microbe symbiosis, such as that between arbuscular mycorrhizal (AM) fungi and many land plants[43,44]. In contrast to many pathogens, AM fungi *Rhizophagus irregularis* appears to lack many GH genes, suggesting that in symbiotic interactions some cell wall modifications essential for microbial accommodation may be undertaken mainly by plant hosts[33,43,44]. Interestingly, a recent study found that a GH81 type β-glucanase, GBP1 from wheat, could enhance colonization of mutualistic fungi including *R. irregularis*[34,45]. It has been also long known that in legume-rhizobial symbiosis, rhizobial infection necessitates extensive cell wall remodeling, but the underlying molecular mechanisms are still obscure[15,18]. In particular, it is not well understood how the IT wall degradation proceeds to allow infection droplet formation and rhizobial release. Similar to the plant cell wall, cellulose, hemi-cellulose and pectin are also present as structural components of IT wall[46,47]. Nodule Pectate Lyase (NPL) was found to degrade pectin and *npl* mutants display abnormal infection phenotype, characterized by large swollen ICs in *L. janponicus*, *M. truncatula* and soybean[48–50]. *NPL* and *symbiosis-specific pectin methyl esterases* (*SyPME1*) also mediate cell wall modifications during IT progression in *M. truncatula* nodules[51]. It has also been reported that a cellulase from *Rhizobium leguminosarum bv. Trifolii*, CelC2, is essential for rhizobial infection in clover[52]. However, it remains unknown whether legume host cellulases are important for rhizobial infection. Here we report that a *M. truncatula* cellulase, Glycoside Hydrolase 9C2 (GH9C2), is required for IT development and rhizobial release.

## Results

### *GH9B3* and *GH9C2* expression pattern is associated with rhizobial infection

Two genes encoding putative cellulases were found from previous Medicago root hair transcriptomic studies[49,53,54]. These belong to the B and C subgroups of the GH9 family[38,39] and were named *GH9B3* (Medtr3g010330) and *GH9C2* (Medtr8g099410) respectively. Their expression in root hairs was specifically induced by *S. meliloti* or Nod factor and their induction was *NODULE INCEPTION* (*NIN*)-dependent (Supplementary Fig. 1a–c). We investigated *GH9B3* and *GH9C2* expression using fusions of their promoters to the GUS gene (*pGH9B3:GUS* or *pGH9C2:GUS*) in composite plants generated via *Agrobacterium rhizogenes* mediated hairy root transformation. X-Gluc staining showed that both genes were expressed in the root tip and lateral root primordia (Supplementary Fig. 1d–g). Upon rhizobial inoculation, they were highly expressed in root hairs, especially in root hairs harboring ITs (Fig. 1a, b). During nodule development, both *GH9B3* and *GH9C2* were highly expressed in nodule primordia, young nodules and in the apical region including the infection zone of mature nodules (Fig. 1a, b). Besides *GH9C2*, there exists another *GH9C* homolog, *GH9C1* (Medtr4g074960), in *M. truncatula*, which was shown previously to be expressed specifically in root hairs[55] and we found that it was also expressed in both root hairs under rhizobial infection and nodules by promoter-GUS analysis (Supplementary Fig. 2). These results show that the symbiotic expression of these *GH9*s are closely associated with the rhizobial infection process.

### *gh9c2* mutants show defective rhizobial infection in both root hairs and nodules

To investigate whether *GH9B3*, *GH9C2* or *GH9C1* is required for rhizobial infection, we isolated *M. truncatula* lines with exonic *Tnt1* insertions, designated as *gh9b3–1* (NF5823), *gh9c1–1* (NF11668) and *gh9c2–1* (NF16578), respectively (Supplementary Fig. 3a–c). Symbiotic phenotypes of these mutants were quantified at 7 dpi (days post inoculation) and 21 dpi with *Sinorhizobium meliloti 1021-lacZ* (Fig. 1c–f, and Supplementary Fig. 3d). At 7 dpi, *gh9b3–1*, *gh9c1–1* and *gh9c2–1* showed similar number of infection events to that of WT (Supplementary Fig. 3d). However, compared to ITs in root hairs in WT, which grew relatively straight and had uniform widths, many ITs in *gh9c2–1* were irregular in shape, and developed swollen segments along their length (Fig. 1c, d). At 21 dpi, while a similar number of pink nodules were found in WT, *gh9c1–1* and *gh9b3–1*, there were very few pink nodules in *gh9c2–1*, and the nodules that formed were mostly small and white (Fig. 1e, f). To test if nitrogen fixation ability in *gh9c2–1* is affected, we inoculated WT and *gh9c2–1* with *S. meliloti 1021-nifH:GUS* and used GUS staining as an indication of *nifH* gene promoter activity, thus, a proxy for rhizobia nitrogenase synthesized. Results from the time course experiment at 14, 21 and 28 dpi showed greatly reduced, if not completely depleted, *nifH* expression in *gh9c2–1* nodules, as expected from their white nodule phenotype (Fig. 1g, h and Supplementary Fig. 4a–i). The nodule phenotype of *gh9c2–1* was further confirmed by complementation experiments (described later in the text). We did RNAi experiments to knock-down *GH9B3* and *GH9C1*, respectively, and no obvious phenotype was found on nodule morphology or nodule numbers (Supplementary Fig. 5a–d). As *gh9b3–1* and *gh9c1–1* didn’t show obvious rhizobial infection or nodule phenotypes, we focused our study on *GH9C2*.

To determine whether rhizobial infection or nodule development is affected in the *gh9c2–1* mutant, we examined its nodules at different developmental stages. Sections of X-Gal stained nodules showed that they were progressively colonized by rhizobia over time in WT (Fig. 2a). In contrast, the nodules of *gh9c2–1* were poorly colonized by rhizobia at all stages (Fig. 2b). In WT mature nodules, rhizobia were present throughout the nodule, with an enrichment of ITs in the infection zone (Fig. 2c). However, at 21 dpi, the nitrogen fixation zone of *gh9c2–1* nodules was often not colonized, ITs were sporadically present, and frequently the rhizobia accumulated intercellularly (Fig. 2d). These abnormal infection structures were also present in nodules at 42 dpi (Supplementary Fig. 6a–c). Further observation confirmed that rhizobial colonization in *gh9c2–1* nodules was severely delayed from an early stage, suggesting that in addition to root hair infection, *GH9C2* also plays a role in nodule infection (Supplementary Fig. 6d–f). Paraffin sections of WT and *gh9c2–1* nodules at 7, 10, 14 and 21 dpi further confirmed defective rhizobial infection and poor rhizobial colonization in *gh9c2–1* nodules (Fig. 2e, f).

### Abnormal IT wall organization in *gh9c2–1* nodules

We hypothesize that GH9C2, as a putative cellulase, may affect the organization of IT wall. Light microscopy revealed the frequent presence of large intercellular infection “blobs” in thin sections of *gh9c2–1* nodules (Supplementary Fig. 7a-c). Further analysis using transmission electron microscopy (TEM) confirmed the accumulation of large

https://doi.org/10.1038/s41467-025-62083-4

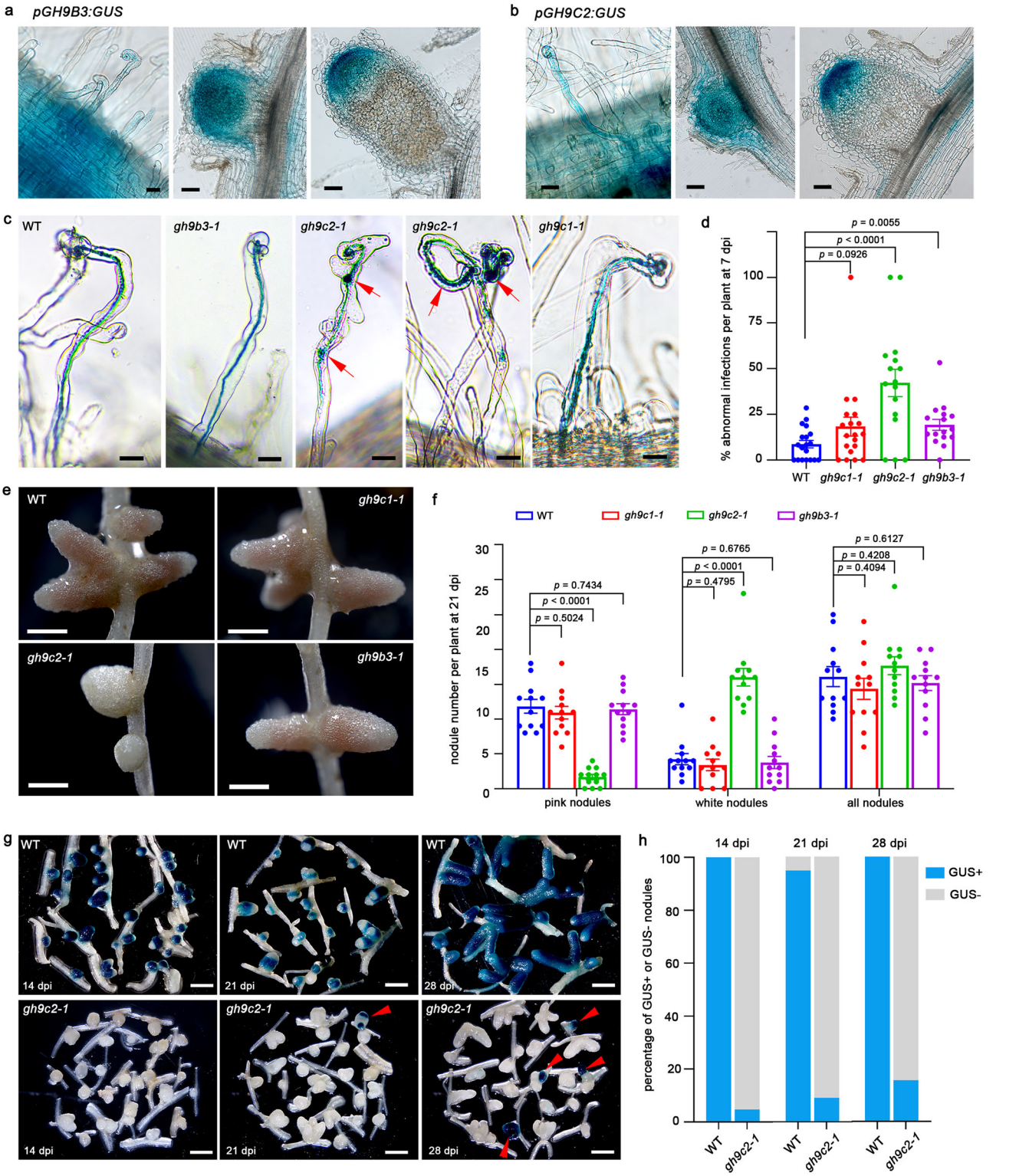


**Fig. 1 | *gh9c2* is defective in rhizobial infection and nitrogen fixation.** **a**, **b** Expression pattern of *GH9B3* and *GH9C2* as shown by promoter-GUS assay. Promoter-GUS assay was repeated twice and at least 22 transgenic plants were analyzed in each experiment. **c** Infection thread phenotypes of WT, *gh9b3-1*, *gh9c1-1* and *gh9c2-1*. Red arrows indicate defective infection threads. **d** Quantification of abnormal rhizobial infection events in WT, *gh9b3-1*, *gh9c1-1* and *gh9c2-1*. N ≥ 16 plants for each genotype. **e** Nodule phenotypes of WT, *gh9b3-1*, *gh9c1-1* and *gh9c2-1*. **f** Quantification of nodule numbers in WT, *gh9b3-1*, *gh9c1-1* and *gh9c2-1*. N = 12 plants for each genotype. Infection and nodulation phenotyping were both repeated three times. **g** GUS staining pattern of WT and *gh9c2-1* at 14, 21 and 28 dpi with *Sinorhizobium meliloti 1021 nifH:GUS*. Red arrowheads indicate residual GUS staining in some *gh9c2-1* nodules. **h** Quantification of GUS assay in **g**. Nodules were randomly selected from 10 plants. N = 62, 58, 59 for WT and 42, 44, 83 for *gh9c2-1* at 14, 21, 28 dpi respectively. nifH:GUS assay was repeated twice. Error bars in (**d**, **f**) indicate SEM. Two-tailed Student's *t*-test. *P* value (**d**): $P = 0.0926$ (*gh9c1-1* versus WT), $P < 0.0001$ (*gh9c2-1* versus WT) and $P = 0.0055$ (*gh9b3-1* versus WT). *P* value (**f**): for pink/white/all nodules, $P = 0.5024/0.4795/0.4094$ (*gh9c1-1* versus WT), $P < 0.0001/ < 0.0001/0.4208$ (*gh9c2-1* versus WT), $P = 0.7434/0.6765/0.6127$ (*gh9b3-1* versus WT). Scale bars, 10 μm, 100 μm and 100 μm (**a**, **b**, from left to right); 20 μm (**c**), 1 mm (**e**) and 2 mm (**g**).

https://doi.org/10.1038/s41467-025-62083-4

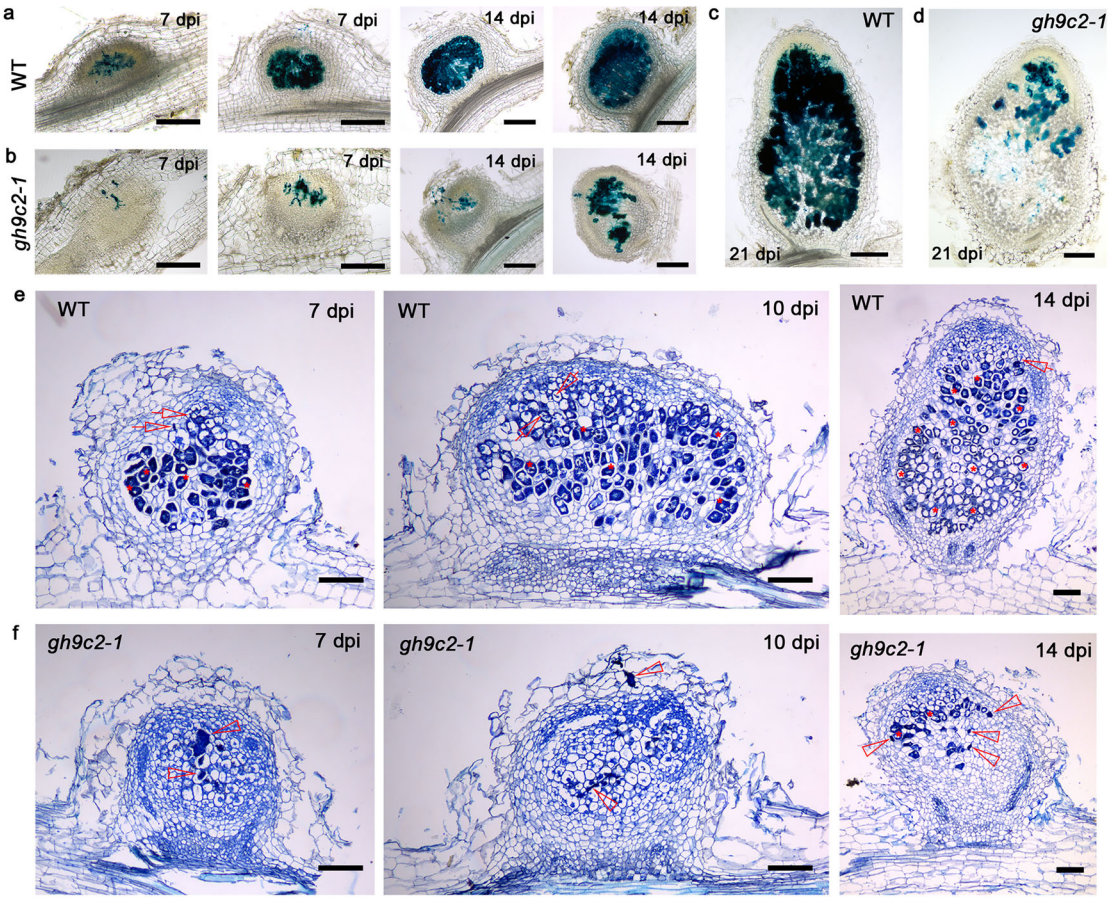


**Fig. 2 | *GH9C2* is required for rhizobial infection and nodule colonization. a, b** Rhizobial infection and colonization shown by X-Gal staining in WT (**a**) and *gh9c2-1* (**b**) nodule primordia and nodules at different stages. Samples were collected at 7 dpi and 14 dpi with *S. meliloti 1021-lacZ*. **c, d** Rhizobial colonization in WT (**c**) and *gh9c2-1* (**d**) at 21 dpi with *S. meliloti 1021-lacZ*. X-Gal staining assay and nodule sections were collected from three independent experiments. N ≥ 18 for WT and N ≥ 16 for *gh9c2-1* at each stage. **e, f** Nodule paraffin sections showing rhizobial infection and nodule colonization in WT (**e**) and *gh9c2-1* (**f**) at different stages. Samples were collected at 7 dpi, 10 dpi and 14 dpi with *S. meliloti 1021-lacZ*. Arrows indicate infection threads in WT nodules (**e**), arrowheads indicate blocked defective rhizobial infections in *gh9c2-1* nodules (**f**), and asterisks indicates some of the nodule cells colonized by rhizobia (**e, f**). Nodules for paraffin sections were selected from 9 plants in two independent experiments. N ≥ 10 for each stage. Scale bars, 200 μm (**a-d**), 100 μm (**e, f**).

amounts of rhizobia within these structures (Supplementary Fig. 8a–b). In contrast, some intercellular infections were also observed in WT nodules, but they were typically smaller and contained only a limited number of rhizobia (Supplementary Fig. 8a). Large intracellular ITs with accumulating rhizobia were also found in *gh9c2–1* nodule cells (Supplementary Fig. 8c). Sometimes degrading symbiosomes were often present in these cells (Supplementary Fig. 8c). Although ITs with abnormally thicker walls were occasionally observed in *gh9c2–1* nodules, quantification of ITs showed that there was no significant difference of their thickness relative to WT (Supplementary Fig. 9). However, clear defects were found in the internal organization of the IT wall in *gh9c2-1* (Fig. 3a–c). Under our experimental conditions, TEM revealed that in WT plants the IT wall displayed a clear pattern with fiber-like structures aligned in parallel along IT cross sections. We hypothesize that these fiber-like structures could be cellulose microfibrils. In contrast, these structures in IT walls of *gh9c2-1* were very disordered and frequently showed variable-sized “gaps” (Fig. 3a–c). These findings indicate that *GH9C2* is required for proper cell wall development, e.g. formation of normal cellulose structure during IT progression.

## Rhizobial release from ITs requires *GH9C2*

Dissolution of the IT wall is a necessary step for rhizobial release into symbiosomes[19]. The sporadic and very weak *nifH-GUS* staining in a few *gh9c2-1* nodules implies that at least some rhizobia are released and develop into symbiosomes, which was confirmed by observation of nodule sections under both light microscopy and TEM (Fig. 1g, h and Supplementary Fig. 7, 10). However, nodule sections showed that symbiosomes were either absent, or present in very limited number of cells in all *gh9c2-1* nodules (Fig. 2 and Supplementary Fig. 7). Hence, we hypothesize that *GH9C2* might be involved in rhizobial release from ITs. We first investigated the rhizobial release process by using TEM to specifically focus on rhizobial release sites in nodule cells (Supplementary Fig. 10). In WT nodules, an unwalled-infection droplet was usually observed to be attached to the infection thread and from the infection droplet rhizobia were released, forming symbiosomes (Fig. 3d, e). In *gh9c2-1* nodule cells, occasionally normal infection droplets could be found (Supplementary Fig. 11). However, in most nodule cells, this pattern was disrupted and the process of rhizobia release was rather chaotic, where enlarged infection threads were often found to be associated with groups of rhizobia (Fig. 3f–h). However, instead of forming an unwalled infection droplet, these groups of rhizobia are surrounded by large fragments of cell walls (Fig. 3g, h). In *gh9c2-1* nodule cells where rhizobia have been released, some abnormal symbiosomes were observed, with cell wall or matrix-like material filling the space between the rhizobia cell wall and symbiosome membrane, in contrast to the very narrow empty spaces as found in WT symbiosomes (Fig. 3e, i). Unlike differentiated symbiosomes in WT, *gh9c2-1* nodule cells also showed large accumulations of

https://doi.org/10.1038/s41467-025-62083-4

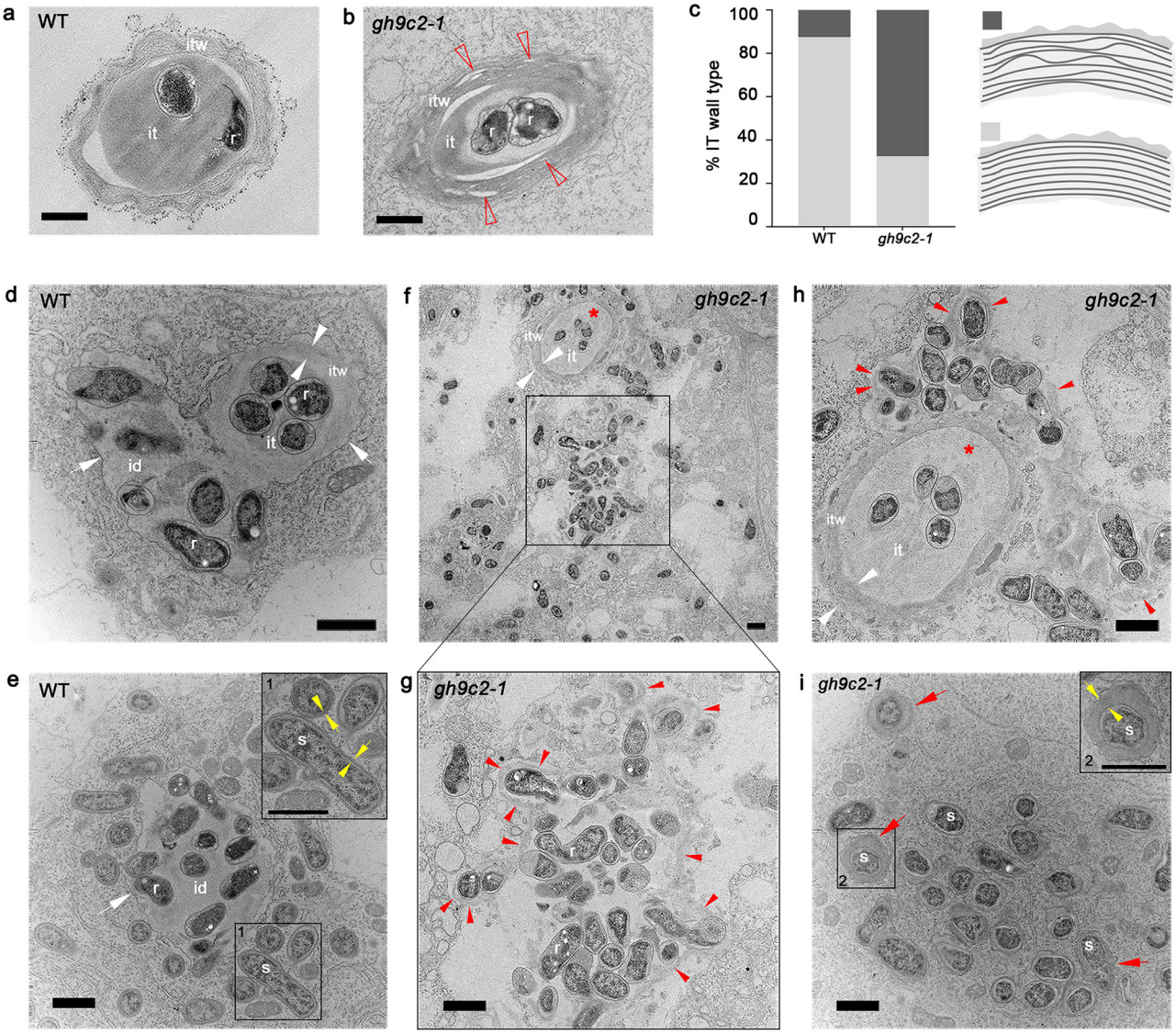


**Fig. 3 | Abnormal rhizobial infection thread wall organization and defective rhizobial release in *gh9c2*.** **a**, **b** Typical intracellular infection thread in WT (**a**) and *gh9c2-1* (**b**). Arrow heads (**b**) indicate gaps in infection thread walls in *gh9c2-1* nodules. **c** Quantification of infection threads with different cell wall organization patterns in WT and *gh9c2-1*. N = 40. Data was collected from more than 10 nodules in two independent experiments. **d** Typical infection thread (it) and an unwalled infection droplet (id) in a WT nodule cell. **e** An infection droplet with some released rhizobia forming symbiosomes. The inlet "1" is the zoomed-in image of the rectangle marked area "1". **f**–**h** Typical rhizobial release foci in *gh9c2-1* nodules. Zoomed-in images are shown in (**g**) for the rectangle-marked region, and (**h**) for the infection thread area (red asterisk) in (**f**), respectively. Image in (**h**) also shows some region not included in (**f**). **i** Defective symbiosome formation in *gh9c2-1* just after rhizobial release. Inlet shows the magnification of the abnormal symbiosome in rectangle-marked region "2". it, infection thread. id, infection droplet. itw, infection thread wall. r, rhizobia. s, symbiosome. White arrowheads indicate the infection thread wall (**d**, **f**, **h**). White arrows indicate the membrane surrounding the infection thread or the infection droplet (**d**, **e**). Red arrowheads indicate residual cell walls in the rhizobial release foci in *gh9c2-1* (**g**, **h**). Red arrows indicate abnormal symbiosomes in *gh9c2-1* (**i**). Yellow arrowheads and yellow arrows indicate bacterial cell wall and symbiosome membrane, respectively (inlets "1" in **e**, "2" in **i**). For rhizobial release phenotyping, TEM was performed using at least 15 nodules from 10 plants in two independent experiments. Scale bars, 100 nm (**a**, **b**), 1 μm (**d**–**i**).

uniformly sized, tightly clustered rhizobia, that were sometimes attached to dense matrix material (Fig. 4a, b). These results show that the process of rhizobial release is also disrupted in *gh9c2-1*.

To further capture the dynamics of rhizobial release in detail and get a quantitative analysis, we resorted to confocal laser scanning microscopy imaging by double staining with Pontamine Fast Scarlet 4B (S4B) dye, which preferentially stains cellulose and has been used for imaging cellulose in Arabidopsis[56] and SYTO-13, for rhizobia in both WT and *gh9c2-1* nodules (Fig. 4e–l). We found that in both WT and *gh9c2-1*, S4B stained both the plant cell wall and IT wall (Fig. 4e-l). This revealed outwardly bulging structures on the IT wall which we here designated as "rhizobial release foci" (Fig. 4e, f, i and Supplementary Fig. 12a). These rhizobial release foci later appeared to develop into unwalled "infection droplets". In addition, S4B staining of the contours of the rhizobial release foci revealed that they appeared to gradually develop sporadic puncta, which we hypothesize could be cell wall/cellulose fragments generated during the process of cell wall/cellulose degradation at these sites before the eventual formation of the unwalled- "infection droplets" for rhizobia release (Fig. 4f, and Supplementary Fig. 12b). In WT, S4B staining gradually disappeared as rhizobial release proceeded, and was completely absent around infection droplets that contained rhizobia (Fig. 4e–h and Supplementary Fig. 12c). But in most *gh9c2-1* nodule cells, S4B staining persisted in the enlarged IT walls and in puncta that partly co-localized with rhizobia (Fig. 4i–l, and Supplementary Fig. 13). Quantification showed that higher percentage of both enlarged rhizobial release foci

https://doi.org/10.1038/s41467-025-62083-4

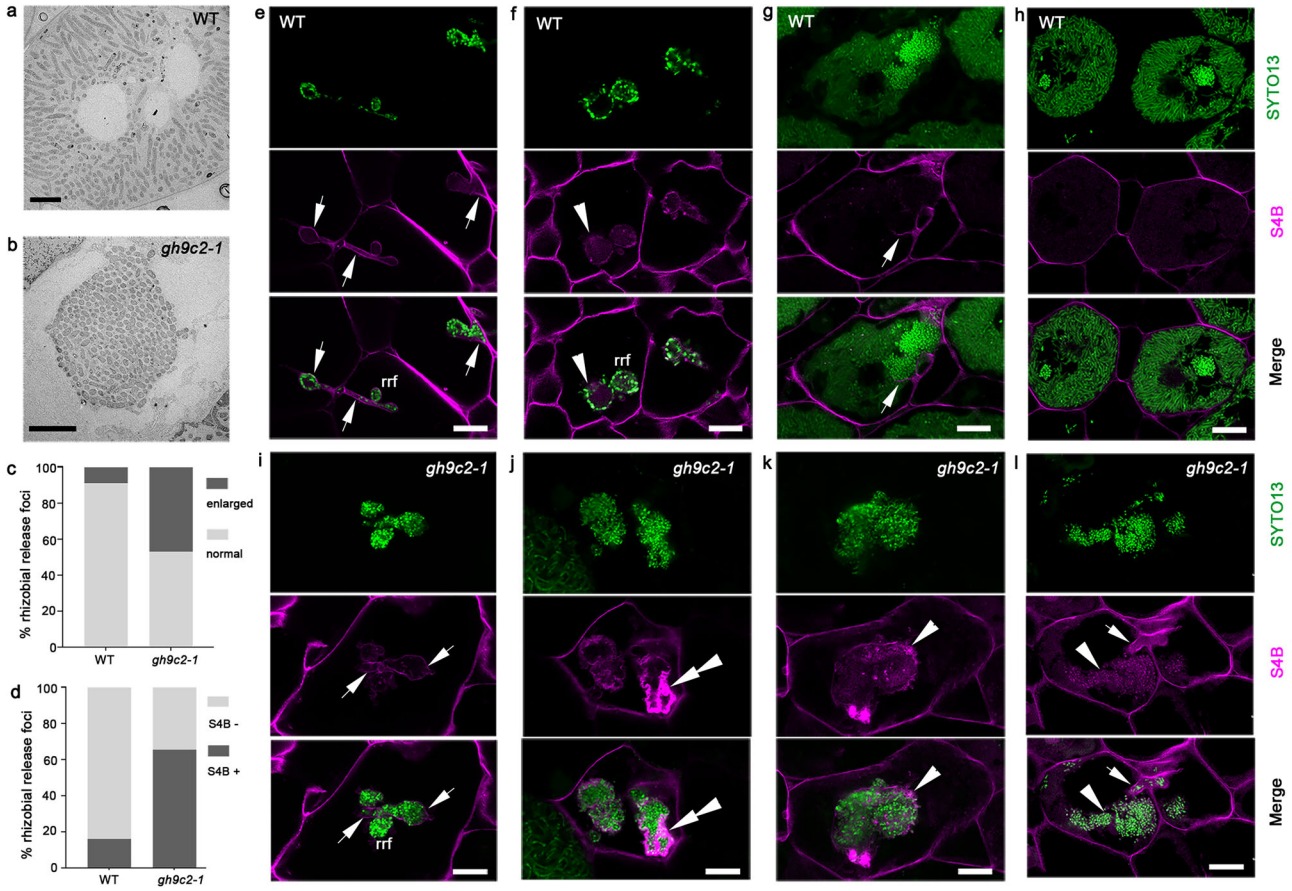


**Fig. 4 | *GH9C2* is required for cellulose degradation during rhizobial release.** **a**, **b** Typical cell of WT (**a**) and *gh9c2-1* (**b**) after rhizobia release from infection threads. **c**, **d** Quantification of enlarged rhizobia release foci (**c**) and presence of S4B staining in rhizobial release foci (**d**) in WT and *gh9c2-1* nodule cells. N = 180 (WT) and 209 (*gh9c2-1*). **e**–**l** S4B staining at different stages of rhizobial release in WT (**e**-**h**) and *gh9c2-1* (**i**-**l**) nodule cells. Rhizobia were stained with SYTO13. Arrows indicate S4B staining in IT wall. Arrowheads indicate S4B staining in rhizobial release foci (**f**, **k**) and cluster of released rhizobia (**l**). Double arrowheads indicate excessive accumulation of S4B staining in *gh9c2-1* (**j**). rrf, rhizobial release foci. For S4B staining assay, rhizobial release phenotyping was collected from three independent experiments, with at least 16 nodules in each experiment. Scale bars, 5 μm (**a**, **b**) and 10 μm (**e**–**l**).

(47% vs 9%) and S4B-stained rhizobia release foci (66% vs 16%) existed in *gh9c2-1*, when compared to that in WT (Fig. 4c, d), suggesting a defective and prolonged process of rhizobial release in *gh9c2-1*. Thus, the S4B staining reveals that rhizobial release is a multi-step process and indicates the involvement of GH9C2, presumably through its degradation of cellulose during rhizobial release (Supplementary Fig. 12d).

## Cellulase activity is required for GH9C2 function during legume-rhizobial symbiosis

We next investigate whether GH9C2 is a bona fide cellulase. Both the full length GH9C2 protein without the N terminal signal peptide and a truncated GH9C2 protein containing only the catalytic domain (CD), $GH9C2^{CD}$ were expressed using a *Pichia pastoris* secretory protein expression system[41,42]. $GH9C2^{CD}$ was successfully expressed, but we were unable to purify the truncated protein, while the full length GH9C2 protein could not be stably detected. Thus, we focused on $GH9C2^{CD}$ and used total protein for cellulase activity assay[57] (Supplementary Fig. 14). Among the different polysaccharides we detected, which include microcrystalline cellulose (MCC), carboxymethylcellulose (CMC), lichenan, arabinan, glucomannan, xylan and pectin, higher enzyme activity was found for MCC and CMC (Fig. 5a). Almost no enzyme activity towards pectin and very weak enzyme activity was found for other polysaccharides (Fig. 5a). This result shows that GH9C2 can degrade cellulose and prefer cellulose for degradation in vitro.

To investigate mutation of *GH9C2* on cell wall composition, we measured content of polysaccharides including cellulose, hemicellulose and pectin, and monosaccharide composition in WT and *gh9c2-1* roots at 14 dpi with *S. meliloti 1021*. The results showed that compared to WT, both cellulose and hemicellulose were reduced, and pectin was increased in *gh9c2-1* (Supplementary Fig. 15a). For monosaccharide composition, glucose was reduced in *gh9c2-1*, consistent with reduced cellulose therein (Supplementary Fig. 15b). Other monosaccharides which showed difference in WT and *gh9c2-1* were mannose and xylose, which had lower and higher content, respectively in *gh9c2-1* (Supplementary Fig. 15b). These results suggest that in addition to cellulose, *GH9C2* may also affect other cell wall components, maybe indirectly.

We further tested whether the function of GH9C2 in nodulation is dependent on its cellulase activity. To this end, we generated constructs for expressing different versions of *GH9C2* with mutations of one, two or three conserved amino acids which were predicted as required for the catalytic activity of GH9C2, i.e., H414, D466 and E475[58–61]. Complementation experiments were performed and the results showed that these mutants were unable to rescue the nodule phenotypes of *gh9c2-1*, suggesting that cellulase activity of GH9C2 is indispensable for its role in the legume-rhizobial symbiosis (Fig. 5b, c).

## GH9C2 location is associated with rhizobial infection and rhizobial release

The subcellular localization of GH9C2 was investigated using a C-terminal GFP fusion driven by either the *pLjUBQ1* promoter or the native *GH9C2* promoter. Live cell imaging in root hairs of composite

https://doi.org/10.1038/s41467-025-62083-4

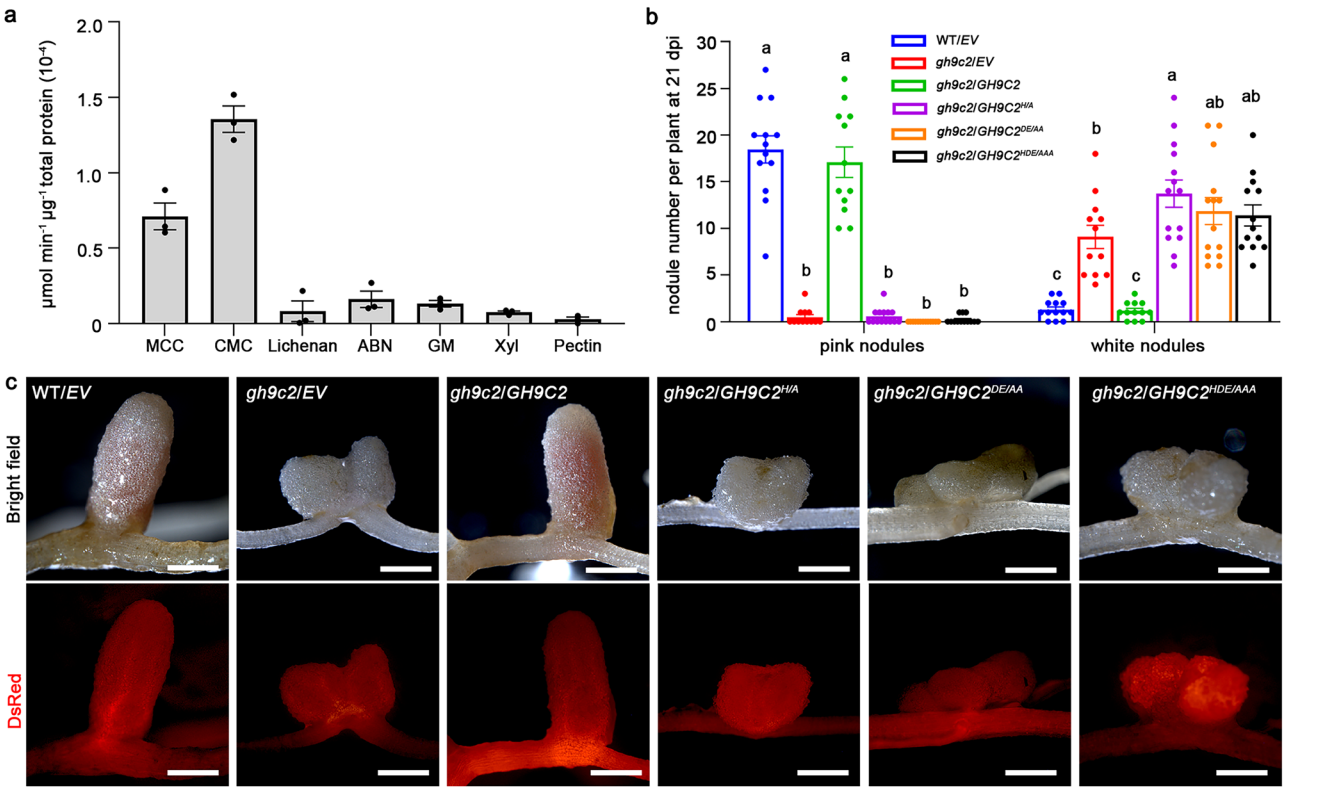


**Fig. 5 | GH9C2 function depends on its cellulase activity. a** Cellulase activity and substrate specificity assay of GH9C2$^{CD}$. Enzyme activity was measured as the amount of reducing sugar (in micromoles) released per minute per microgram of total protein, using the 3,5-dinitrosalicylic acid (DNS) method. Total protein was incubated with different substrates at optimal pH and optimal temperature. Total protein from empty vector transformants was used as negative control to subtract background. MCC, microcrystalline cellulose; CMC, carboxymethylcellulose; ABN, arabinan; GM, glucomannan; Xyl, xylan. Substrate specificity assay was performed more than four times and similar results were observed. A representative result from one experiment was shown in (**a**) and dots indicate the values of three technical replicates. **b**, **c** Quantification of nodule numbers (**b**) and typical nodule phenotype (**c**) in WT plants transformed with empty vector (*EV*), *gh9c2*-1 transformed with *EV*, *GH9C2*, or *GH9C2* with one, two or three amino acids mutated. DsRed was used as a transgenic marker. Error bars indicate SEM. Multiple comparison tests were performed using a one-way ANOVA followed by the Turkey's post-hoc test. Letters were assigned to indicate statistically significant differences (adjusted $P \leq 0.05$) of varying degrees. N ≥ 12 plants. The experiment was repeated twice and similar results were observed. Scale bars, 1 mm.

plants transformed with the *pLjUBQ1:GH9C2-GFP* construct showed that GH9C2-GFP localized to the tips of initiating and elongating root hairs (Supplementary Fig. 16a). Replacement of GFP with mCherry in the construct exhibited the same tip-localized pattern. This tip-localized GH9C2-mCherry signal was also maintained in plasmolyzed root hairs, showing that GH9C2 is localized to the cell wall rather than to the plasma membrane (Supplementary Fig. 16b). After rhizobial inoculation, the GH9C2-GFP signal was also found in infection chambers and infection threads (Supplementary Fig. 16c, d). In line with GH9C2's role in rhizobial infection, GH9C2-GFP driven by the native *pGH9C2* promoter was found to localize to ICs and ITs in root hairs, but didn't localize to root hair tips, which indicates that native promoter may confer GH9C2 a more stringent localization pattern during legume-rhizobial symbiosis (Fig. 6a–d).

GH9C2 localization was further investigated in nodules of *pGH9C2:GH9C2-GFP* composite plants. GH9C2-GFP signal was found in ITs of developing nodules (Fig. 6e). In mature nodules with clear zonation, GH9C2-GFP was conspicuously localized to ITs in the distal infection zone, where IT growth and rhizobial release are most active (Fig. 6f, g). GH9C2-GFP also localized to the apoplastic regions between cells at sites of IT passage (Fig. 6h–j and Supplementary Fig. 17a). The GH9C2-GFP signal in ITs gradually weakened along the apical-basal axis into the proximal infection zone, and in cells where rhizobial release occurs, it was found in IT bulges representing incipient rhizobial release foci (Fig. 6h–j and Supplementary Movie 1). In cells where rhizobia were undergoing release, GH9C2-GFP signal accumulated at rhizobial release foci, especially in infection droplets (Fig. 6j, k and Supplementary Fig. 18). More interestingly, GH9C2-GFP was also localized as puncta, which stayed close to, but not completely overlapped with newly released rhizobia (Fig. 7a, and Supplementary Fig. 17b, Supplementary Fig. 19a-c). GH9C2-GFP was also associated with differentiating rhizobia, although at a seemingly lower level, and was also present in some compartments, likely vacuoles (Fig. 7b). The GH9C2-GFP localization is reminiscent of the S4B-stained cellulose distribution pattern in nodule cells containing rhizobial release foci, including infection droplets, consistent with the defects of rhizobial release in *gh9c2-1* (Fig. 3d–i, Fig. 4e–l, Fig. 6h–k, Fig. 7c–e, and Supplementary Figs. 17b, 19). Similar localization results were observed in both WT and *gh9c2-1* plants transformed with *pGH9C2:GH9C2-GFP*. Our effort to further investigate the possible co-localization of S4B staining puncta and GH9C2-GFP was failed and it seemed that the GFP was immediately quenched by S4B. We further tried another cell wall fluorescence dye, Calcofluor White, for the double staining. We found that some Calcofluor White-stained puncta could co-localize with GH9C2-GFP during rhizobial release (Supplementary Fig. 20a–c). These results indicate that GH9C2 functions in both IT progression and rhizobial release by degrading cellulose materials as part of the cell wall remodeling process, which is essential during the legume-rhizobial symbiosis.

## CBM49 domain contributes differentially to rhizobial infection and rhizobial release

All GH9 proteins contain a glycosidase domain and GH9C proteins also have an additional carbohydrate binding domain, CBM49 (Fig. 8a). To

https://doi.org/10.1038/s41467-025-62083-4

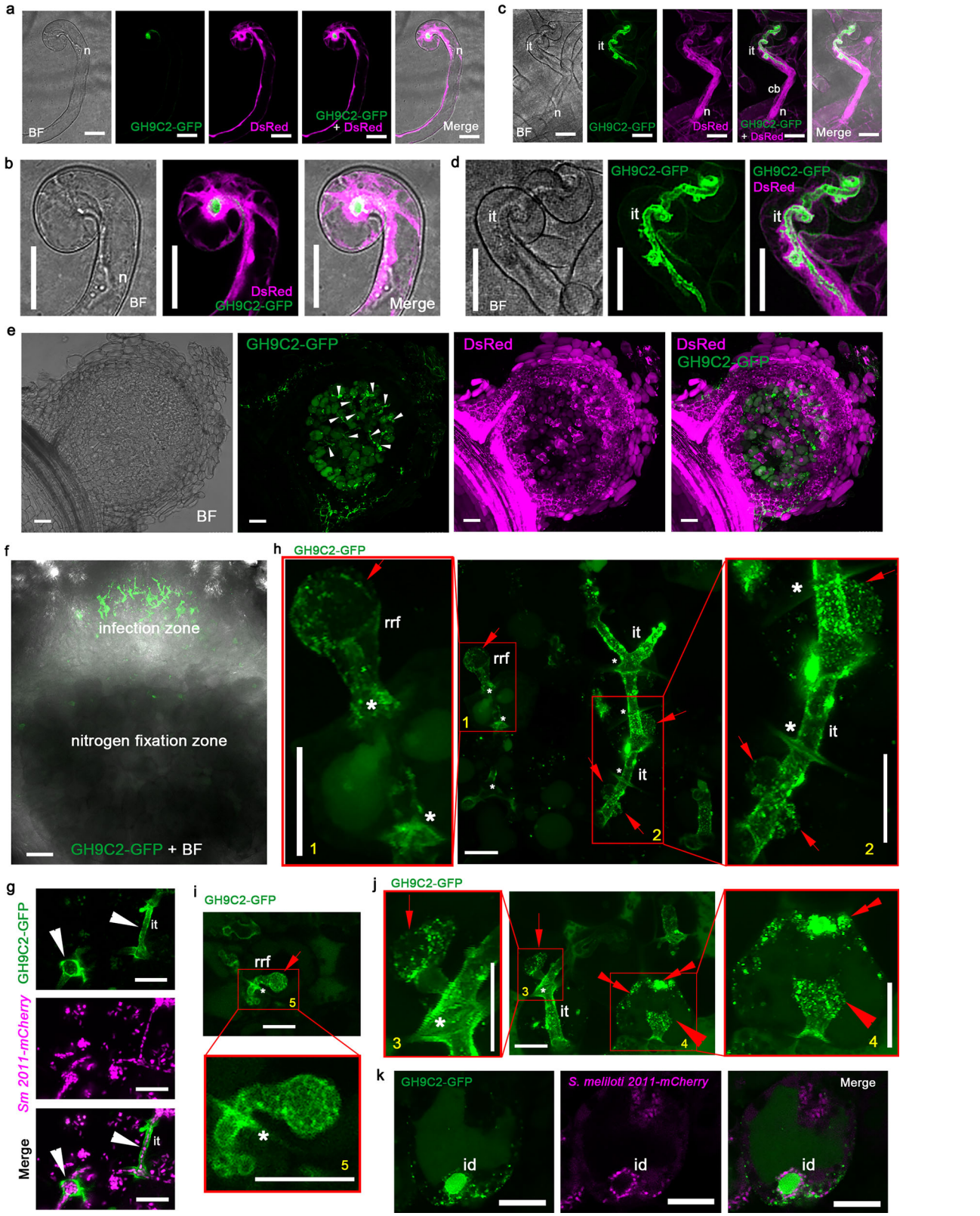


test whether CBM49 domain is essential for GH9C2 subcellular localization, we transgenically expressed a GFP fusion of GH9C2 lacking its CBM49 domain (GH9C2$^{\Delta CBM49}$) (Fig.8a). Live cell imaging in root hairs showed that GH9C2$^{\Delta CBM49}$ failed to localize to root hair tips, contrasting with the full length GH9C2, when driven by *LjUBQ1* promoter (Supplementary Fig. 21a). In all root hairs, GH9C2$^{\Delta CBM49}$ accumulated in puncta associated with nucleus, which was never seen for GH9C2, which may reflect a defect in the secretion of GH9C2$^{\Delta CBM49}$ (Supplementary Fig. 21a, b). However, GH9C2$^{\Delta CBM49}$ was still able to localize to ITs in root hairs, either driven by *LjUBQ1* or the native promoter (Fig. 8b and Supplementary Fig. 21c). In nodules, GH9C2$^{\Delta CBM49}$-GFP accumulated at rhizobial release foci/infection droplets, showed punctate association with newly released rhizobia, and localized to the apoplastic region of cell junctions, a pattern similar to GH9C2-GFP

**Fig. 6 | Subcellular localization of GH9C2 in infected root hairs and nodule cells. a–d** GH9C2-GFP localization in the infection chamber (**a**–**b**) and infection thread (it, **c**–**d**) in root hairs. n, nucleus. cb, cytoplasmic bridge. Zoomed-in images of the root hair region with infection chamber (**a**) or it (**c**) are shown in **b** and **d**, respectively. **e** Localization of GH9C2-GFP in infection threads (arrowheads) in young nodules. **f** Localization of GH9C2-GFP in the distal region of infection zone in nodules. **g-j**, Localization pattern of GH9C2-GFP during infection thread development and rhizobia release in infected nodule cells. White arrowheads indicate infection threads in nodules (**g**).Red arrows indicate incipient rhizobial release foci bulging from infection threads (**h-j**). White asterisks indicate junctions between cells (**h**–**j**). Red arrowhead indicates the site of rhizobial release (**j**). Double arrowheads indicate punctate accumulation of GH9C2-GFP in a rhizobia-releasing cell (**j**). Zoomed-in images of regions in h-j (red rectangular) are shown and are numbered from 1 to 5 (**h**–**j**). **k** Accumulation of GH9C2-GFP in infection droplets (id). *GH9C2-GFP* was driven by native *GH9C2* promoter (**a**–**k**). Free DsRed was used to mainly image cytoplasm and nucleus (**a**–**e**). GH9C2-GFP localization in root hairs and nodules was both investigated in three independent experiments. At least 50 root hair infection events ("ic" plus "it") were observed from 10 transgenic plants in each experiment. More than 15 nodules from 10 transgenic plants were selected for GH9C2-GFP nodule localization in each experiment. Scale bars, 20 μm (**a**–**d**), 50 μm (**e**, **f**) and 10 μm (**g**–**k**).

(Fig. 8c, d and Supplementary Fig. 21d). However, IT localization of GH9C2$^{\Delta CBM49}$ was hardly observed in nodules (Fig. 8d, Supplementary Fig. 22). This result indicates that CBM49 is indispensable for GH9C2 localization to ITs in nodules.

Rhizobial infection and rhizobial release are both essential for nodule colonization by rhizobia, transporting and unloading rhizobia, respectively. To test the functional relevance of CBM49 domain in these two processes, we conducted complementation experiment on *gh9c2-1* using constructs of different forms of *GH9C2*, including another one lacking CBM49 (GH9C2.2), driven by the native *GH9C2* promoter (Fig. 8a). The results showed that *gh9c2-1* formed as many total nodules as WT, when transformed with either *GH9C2*, *GH9C2$^{\Delta CBM49}$* or *GH9C2.2* at 28 dpi, while *GH9B3* couldn't restore pink nodule on *gh9c2-1* (Supplementary Fig. 23a, b). However, further examination of nodule sections at 14 dpi showed that GH9C2 lacking the CBM49 domain could not fully complement the nodule colonization phenotype (Fig. 8e, f). To further dissect whether the colonization defects are due to defective rhizobial infection, we quantified infection events at 14 dpi. The results showed that although total infection events were not affected (Supplementary Fig. 23c), *gh9c2-1* transformed with truncated GH9C2 developed defective ITs like those of *gh9c2-1* mutants, and only full length GH9C2 could complement the rhizobial infection phenotype (Fig. 8g, h). Our results indicate that the glycosidase domain of GH9C2 is necessary and sufficient for rhizobial release, while the CBM49 domain is indispensable for rhizobial infection (Supplementary Fig. 24).

### GH9C2, GH9C1 and NPL act synergistically in the legume-rhizobial symbiosis

Although ITs were defective in *gh9c2-1*, many could still progress into developing nodules from root hairs. This leads us to speculate whether the only homolog of *GH9C2 in M. truncatula*, *GH9C1*, which is highly expressed in epidermis[55], is also involved in rhizobial infection. Investigation of the mutant revealed that the root hairs of *gh9c1-1* were shorter and wider than those of WT (Supplementary Fig. 25a–d), and that this phenotype could be rescued by *GH9C1* (Supplementary Fig. 25e, f). In line with this, GH9C1-GFP driven by *pGH9C1* promoter localized to the tips of initiating and elongating root hairs (Supplementary Fig. 26a, b). GH9C1-GFP was also found in ICs but not in ITs in root hairs and nodules (Fig. 9a and Supplementary Fig. 27). We made a double mutant and found that compared to *gh9c2-1*, there were more abnormal enlarged microcolonies in *gh9c1-1 gh9c2-1* (Fig. 10 and Supplementary Fig. 28). This suggests that *GH9C1* is also involved in rhizobial infection, mainly contributing to the formation of ICs.

NPL is a pectin degrading enzyme shown to be involved in rhizobial infection which localizes to both ICs and ITs in *M. truncatula*[49,51]. We found that NPL-GFP and GH9C2-tdTomato, both driven by their native promoter, co-localized in ICs and ITs in root hairs, also at the tips of newly initiated IT branches in nodules (Fig. 9b–c, and Supplementary Fig. 29a). This co-localization pattern was confirmed using GH9C2-GFP and NPL-tdTomato (Fig. 9d, andSupplementary Fig. 29b, 30). To test if there is genetic interaction between *GH9C2* and *NPL*, we made a double mutant (Fig. 10 and Supplementary Fig. 28). Similar to *npl-1*, *gh9c2-1 npl-1* had more enlarged microcolonies and greatly reduced number of elongating ITs in root hairs (Supplementary Fig. 28). Moreover, number of nodule plus nodule primordia in *gh9c2-1 npl-1* was significantly reduced in comparison to that of *npl-1* or *gh9c2-1* single mutant, consistent with delayed progression of rhizobial infection in *gh9c2-1 npl-1* (Fig. 10d, e). To further test whether NPL functions in later stages of rhizobial infection and rhizobial release, we inoculated WT, *gh9c2-1*, *npl-1* and *gh9c2-1 npl-1* with *S. meliloti 1021-nifH:GUS* and quantified the GUS staining at 14, 21 and 28 dpi. Compared to WT, *npl-1* showed reduced percentage of GUS-stained nodules, more obviously at an earlier stage at 14dpi (Supplementary Fig. 31). This phenotype of *npl-1* was much weaker than that of *gh9c2-1* and at 28 dpi, the difference between WT and *npl-1* became subtle (Supplementary Fig. 31). The percentage of GUS-stained nodules in *gh9c2-1* was slightly decreased in *gh9c2-1 npl-1*, consistent with a slight increase in the percentage of S4B-stained rhizobial release foci in *gh9c2-1 npl-1*, though the percentage of abnormal rhizobial release foci were not changed (Supplementary Fig. 31, 32). Similar to that WT and *gh9c2-1*, normal differentiated symbiosomes did form in *gh9c2-1 npl-1* (Supplementary Fig. 33). These results suggest that *NPL* may play a minor role in rhizobial release and mainly functions in rhizobial infection, together with *GH9C2*.

## Discussion

In root nodule symbiosis, the host-made IT conveys rhizobia into nodule cells[62]. The IT wall, formed by the inward growth of the plant cell wall, the main barrier to microbial invasion, functions as a protection for both symbiotic partners, allowing the rhizobia to traverse several root and nodule cell layers[18,63,64]. However, it constitutes a formidable barrier for rhizobia to overcome when the IT reaches the destination cell where rhizobia are being unloaded. At this stage, the dissolution of IT wall is essential to secure rhizobial release from the IT in legume nodules that harbor symbiosomes (SYM type nodules), the innovation of which is thought to provide the evolutionary stability of nitrogen fixation in legumes[64]. We find that *M. truncatula GH9C2* plays dual roles in IT development and rhizobial release, likely by degrading cellulose and other polysaccharides. Our finding provides a clear evidence that cellulase from the legume host is indispensable for rhizobial colonization in root nodule symbiosis.

Compared to rhizobial infection, host regulation of rhizobial release is relatively underexplored and our understanding of the related molecular mechanisms is minimal[10,11,19,65]. In many legume mutants that are defective in rhizobial infection, the ITs rarely reach nodule cells, which masks the potential roles that the related proteins may play in rhizobial release[66–69]. In *gh9c2-1*, even though clear defective ITs are found and the process of rhizobial infection is largely delayed, many ITs eventually penetrate into nodules, revealing a defect in rhizobial release (Figs. 1–3). Our findings reveal that cell wall degradation initiates at small foci that bulge from ITs and persists until rhizobia are released and differentiate to some extent (Figs. 4, 6). We propose "rhizobial release foci" as transient structures formed in the process of rhizobial release, to distinguish them from the un-walled infection droplets. However, it should be noted that rhizobial release

https://doi.org/10.1038/s41467-025-62083-4

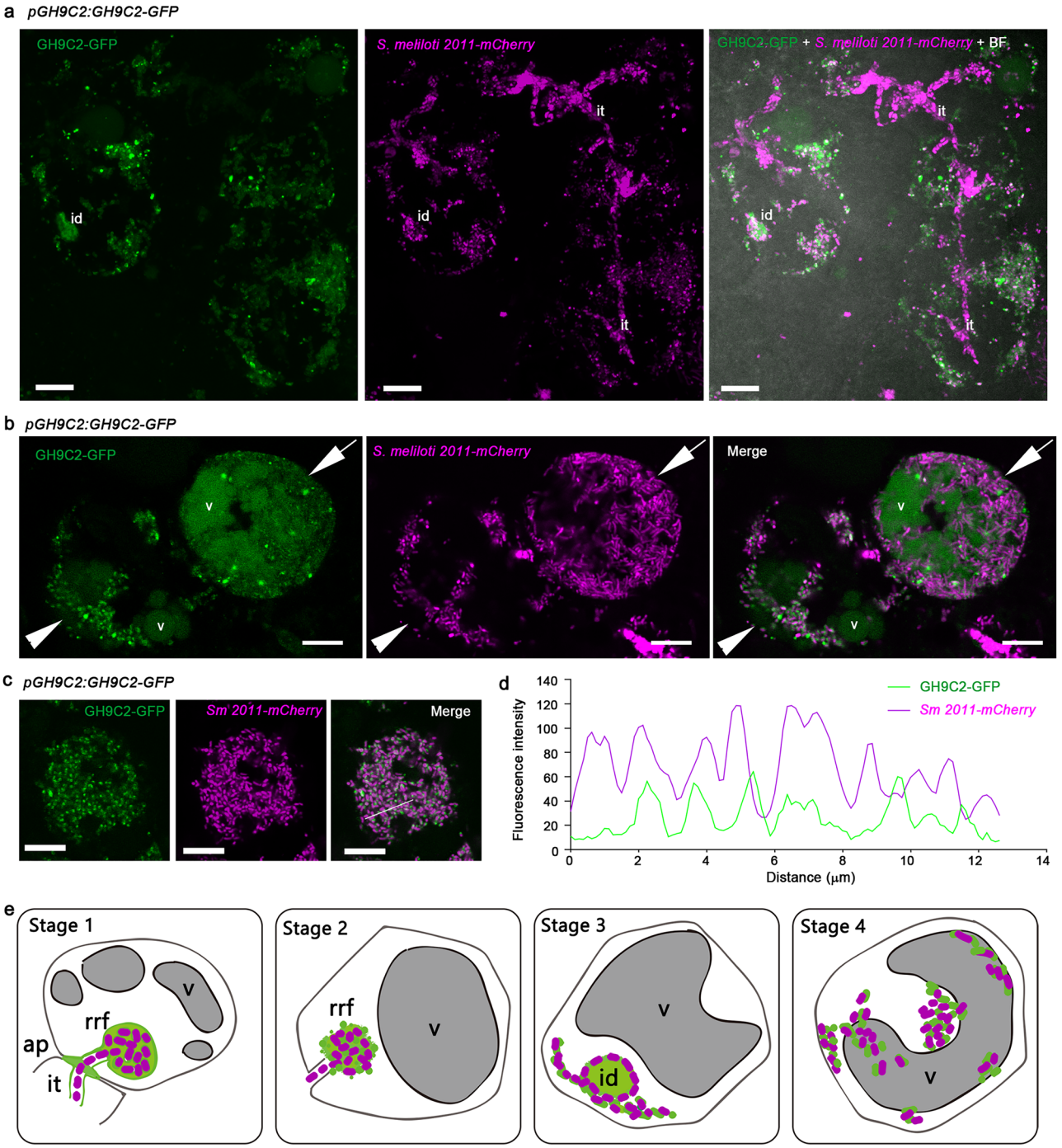


**Fig. 7 | Subcellular localization of GH9C2 is associated with released rhizobia.** **a** Accumulation of GH9C2-GFP in infection droplets (id) and as puncta associated with released rhizobia in infected nodule cells. it, infection thread. **b** In cells with differentiating rhizobia (arrow), the punctate GH9C-GFP signal associated with released rhizobia (arrowhead) is relatively weak, and is frequently found in the vacuole-like compartments. **c**, **d** Analysis of co-localization of GH9C2-GFP with *S. meliloti 2011-mCherry*. The white line in the "Merge" panel indicates the signals for analysis in **c**. *GH9C2-GFP* was driven by native *GH9C2* promoter (**a**–**d**). Scale bars, 10 μm. **e** Illustration of the process of rhizobia release along with GH9C2 subcellular localization at different stages. Green color indicates GH9C2, which localizes to both the IT and developing rhizobial release focus at stage 1, and to the rhizobial release focus including the infection droplet and/or released rhizobia from stage 2 onwards. Magenta color indicates rhizobia. it, infection thread. rrf, rhizobial release foci. id, infection droplet. ap, apoplastic region. v, vacuole-like compartments. GH9C2-GFP localization in nodules was investigated in three independent experiments. More than 15 nodules from 10 transgenic plants were selected for GH9C2-GFP nodule localization observation in each experiment.

foci are mainly quantified by their morphology and there is possibility that some of them might be a result of defective rhizobial infection, e.g. abnormal IT branching, rather than a direct effect of defective rhizobial release, as both processes occur in distal infection zone and both are affected in *gh9c2-1* mutant. Due to the technical impossibility to trace the live process of rhizobial release in nodules, some of these "foci" may not proceed to form infection droplets. Additional molecular markers and co-imaging of both membrane and cell wall proteins are needed in future to further elaborate the transition from elongating/branching IT to un-walled infection droplets. GH9C2 secures the

https://doi.org/10.1038/s41467-025-62083-4

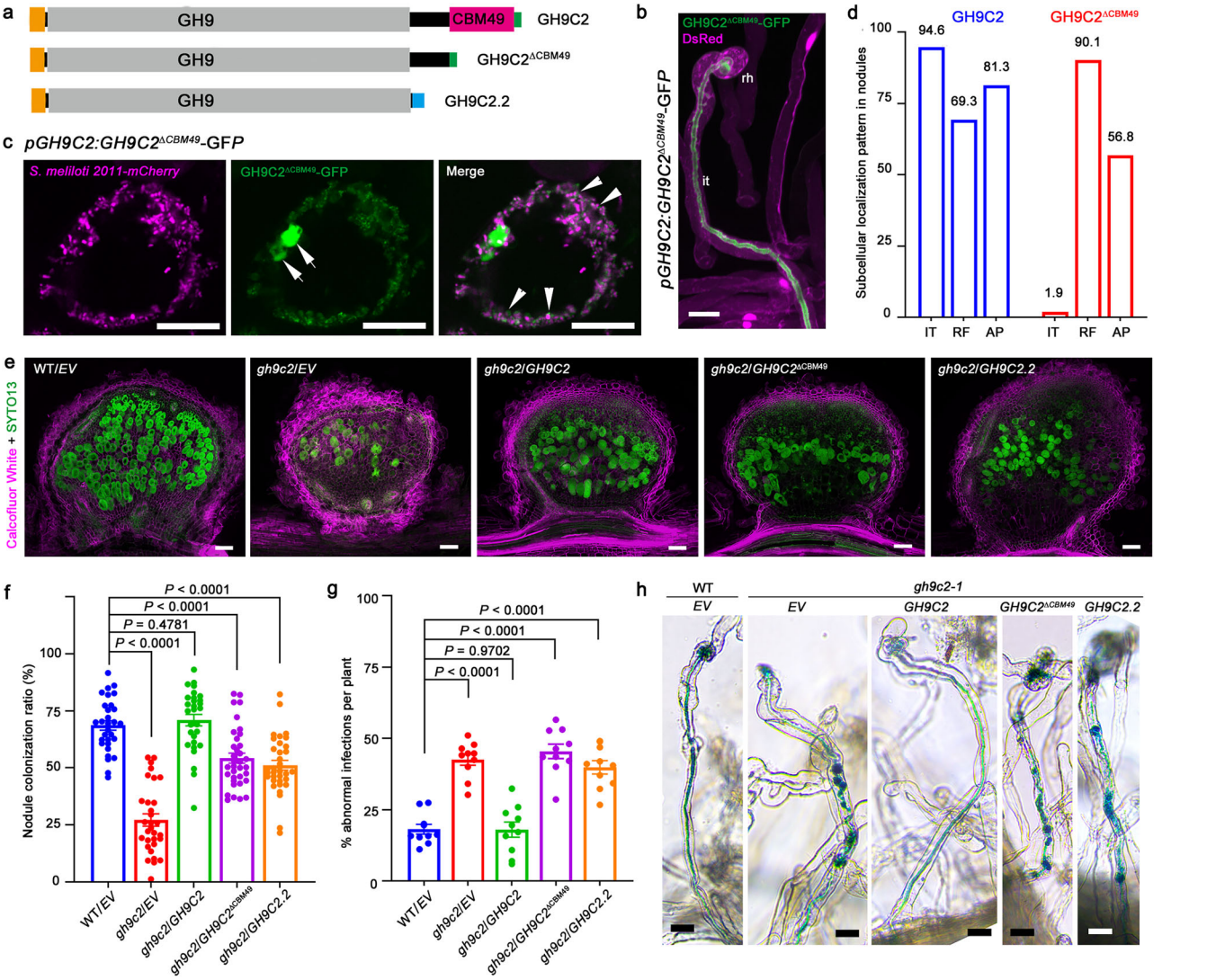


**Fig. 8 | The CBM49 domain of GH9C2 differentially contributes to rhizobial infection and rhizobial release. a** Illustration of full length (GH9C2) and truncated GH9C2 (GH9C2$^{\Delta CBM49}$, GH9C2.2) used for complementation experiment. **b** Localization of GH9C2$^{\Delta CBM49}$-GFP to the infection thread (it) in root hairs (rh) observed in *pGH9C2:GH9C2$^{\Delta CBM49}$-GFP pAtUBQ10:DsRed* hairy roots. Free DsRed was used to mainly image cytoplasm and nucleus (**b**). Root hair localization of GH9C2$^{\Delta CBM49}$-GFP was investigated in two independent experiments. At least 32 infection threads were observed from 10 transgenic plants in each experiment. **c** Typical localization of GH9C2$^{\Delta CBM49}$-GFP at the rhizobial release foci/infection droplet (arrows) and associated with released rhizobia (arrowheads) in an infected nodule cell. Magenta color indicates mCherry tagged *S. meliloti 2011*. Similar results were observed in three independent experiments, with at least 15 nodules investigated in each experiment. **d** Quantification of GH9C2-GFP and GH9C2$^{\Delta CBM49}$-GFP subcellular localization patterns in nodules. IT, infection thread. RF, rhizobial release foci. AP, apoplastic region between cells. The percentage of each localization pattern observed in total nodules is indicated above the corresponding column. Nodules used for quantification were from transgenic plants in 7 independent experiments. N = 75 for GH9C2-GFP and 51 for GH9C2$^{\Delta CBM49}$-GFP. **e** Typical rhizobial nodule colonization pattern from *gh9c2-1* complementation experiment. Nodule sections were double stained with Calcofluor White (magenta) for cell wall and SYTO13 for rhizobia (green). **f**, **g** Quantification of nodule colonization ratio (**f**) and abnormal infection events ratio (**g**) for the complementation experiment. Error bars indicate SEM. Two-tailed Student's *t*-test. *P* value (**f**): $P < 0.0001$, $P = 0.4781$, $P < 0.0001$ and $P < 0.0001$ for different genotypes versus WT/*EV* respectively. *P* value (**g**): $P < 0.0001$, $P = 0.9702$, $P < 0.0001$ and $P < 0.0001$ for different genotypes versus WT/*EV* respectively. N ≥ 29 nodules (**f**). N = 10 plants (**g**). **h** Root hair infection threads could not be complemented by *GH9C2$^{\Delta CBM49}$*, nor *GH9C2.2*. Complementation assay was repeated twice. Samples were collected at 14 dpi with *S. meliloti 1021-lacZ* (**e**–**h**). Scale bar, 20 μm (**b**, **h**), 15 μm (**c**), 100 μm (**e**).

progression of this multi-step rhizobial release and its function in this process does not rely on the CBM49 domain. The CBM49 domain of SlGH9C in *Solanum lycopersicum* was shown to bind crystalline cellulose[38]. It is currently unknown whether different forms of cellulose are predominant in different locations and at different stages of rhizobial symbiosis. We tried to image a fluorescent protein-CBM3a fusion and found that YPet-CBM3a showed nodule IT labeling, as well as punctate labeling in rhizobia-releasing nodule cells, suggesting the presence of crystalline cellulose (Supplementary Fig. 34a–d). However, it still awaits future exploration by using more different CBM labeling to clarify exact cellulose composition during rhizobial infection and rhizobial release[70]. The differential requirements for the CBM49 domain in rhizobial infection and rhizobial release may reflect distinct cellulase actions which are required in these two processes. The typical "bulbs" in *gh9c2* IT walls suggests that IT formation is finely regulated, which presumably requires the specially localized GH9C2 activity therein to hydrolyze the β-1,4-glycosidic bond, to make a well-structured IT wall as seen in WT. Building ITs is such a delicate cell wall remodeling process that requires certain stringency, presumably provided by the CBM49 domain. On the other hand, rhizobial release

https://doi.org/10.1038/s41467-025-62083-4

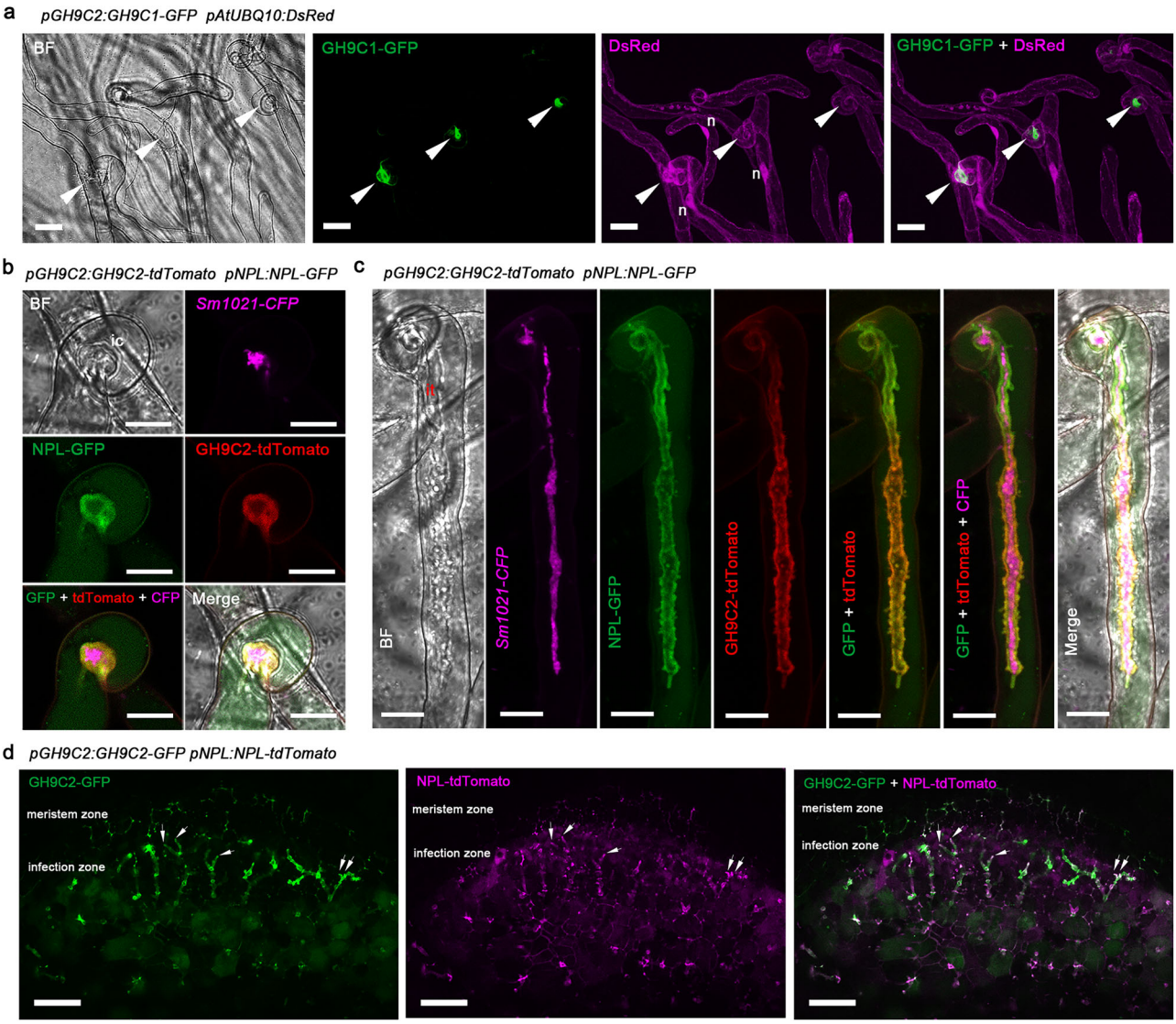


**Fig. 9 | Subcellular localization of GH9Cs and NPL during rhizobial infection.** **a** Imaging of GH9C1-GFP in infection chambers (arrowheads). Free DsRed was used to mainly image cytoplasm and nucleus (n). Similar results were obtained in two independent experiments, with more than 28 infection events observed from 10 transgenic plants in each experiment. **b**, **c** Co-localization GH9C2-tdTomato and NPL-GFP in IC (**b**) and IT in root hairs (**c**). ic, infection chamber. it, infection thread. Similar results were obtained in two independent experiments, with at least 54 infection events observed from 12 transgenic plants in each experiment. **d** Co-localization GH9C2-GFP and NPL-tdTomato in ITs in the nodule infection zone. White arrows (**d**) indicate tips of branching infection threads. This experiment was repeated twice, with 20 nodules collected from at least 10 transgenic plants in each experiment. All constructs were driven by native promoter. Scale bars, 20 μm (**a**), 10 μm (**b**, **c**) and 60 μm (**d**).

involves rather non-selective cell wall degradation which GH9C2$^{\Delta CBM49}$ would suffice. However, the specific impact of the GH9C2 catalytic domain on cellulose structure and the biochemical function of the CBM49 domain, especially during the processes of rhizobial infection and rhizobial release, awaits further investigation.

Here we used S4B for imaging cellulose and we could not rule out that other cell wall components may also be relevant during rhizobial infection and rhizobial release in *gh9c2-1*. Although so far reported plant GH9Cs degrade cellulose efficiently, they could degrade other polysaccharides in vitro[38,41,42]. Our results showed that GH9C2$^{CD}$ had much higher specificity for cellulose in vitro. Cell wall composition assay showed that cellulose and glucose were the most affected polysaccharides and monosaccharides in whole nodulated roots of *gh9c2-1*. It should be noted that this result could not reflect the very specialized local changes of cell wall composition, such as in infection threads or at rhizobial release foci, which is hard to quantify due to technical difficulty. It is possible that GH9C2 can degrade other carbohydrates *in planta*, in addition to cellulose, and these carbohydrates may have differential distribution in infection threads in nodules and root hairs.

The *M. truncatula* genome encodes more than 30 *GH9s* and only two of them are *GH9Cs*, constituting the *GH9C1* and *GH9C2* clades, as in most flowering plants (Supplementary Figs. 35, 36, 37; and Supplementary Data 1, 2, 3). Unlike the root and rhizobial induced expression of *GH9C2*, *GH9C1* is specifically expressed in epidermis under non-symbiotic condition and *gh9c1* shows root hair developmental defects, similar to its ortholog in Arabidopsis[55,71]. GH9C1 also localizes to ICs, but notably it is not found in ITs, a pattern different from GH9C2 or NPL, which localizes to both ICs and ITs, indicating that distinct components are involved in IC formation and IT development. It has been shown that NPL and SyPEM1 function at the cell to cell passage of infection threads, protein localization and nodule infection phenotype suggest that GH9C2 also play a role at this so called "transcellular passage cleft", or TPC[51,72]. More cell wall enzymes are expected to be found at TPC, and thus, a cohort of cell wall players is deployed here for targeting different cell wall components for modification/

https://doi.org/10.1038/s41467-025-62083-4

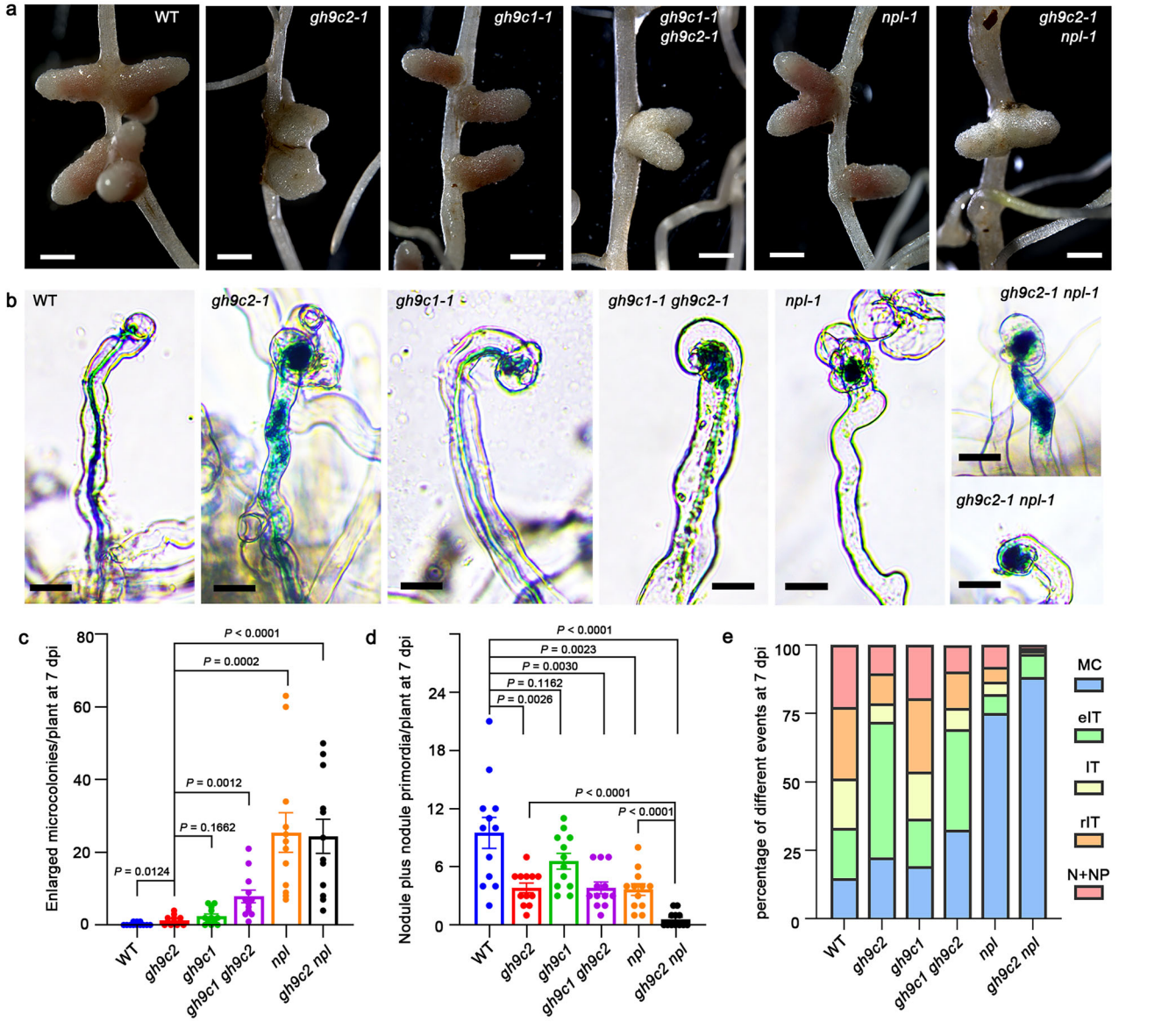


**Fig. 10 | Synergistic effects of *GH9Cs* and *NPL* on rhizobial infection. a**, **b** Nodules at 21 dpi (**a**) and rhizobial infection phenotypes at 7 dpi (**b**) of WT, *gh9c2-1*, *gh9c1-1*, *gh9c1-1 gh9c2-1*, *npl-1* and *gh9c2-1 npl-1*. **c**–**e** Quantification of enlarged microcolonies (**c**), nodule plus nodule primordia (**d**) and total infection events (**e**) of WT, *gh9c2-1*, *gh9c1-1*, *gh9c1-1 gh9c2-1*, *npl-1* and *gh9c2-1 npl-1* at 7 dpi with *S. meliloti 1021-lacZ*. MC, microcolony. eIT, elongating infection thread. IT, infection thread. rIT, ramified infection thread. N + NP, nodule plus nodule primordia. Error bars indicate SEM. Two-tailed Student's *t*-test. *P* value (**c**): $P = 0.0124$ (*gh9c2* versus WT), $P = 0.1662$ (*gh9c1* versus *gh9c2*), $P = 0.0012$ (*gh9c1 gh9c2* versus *gh9c2*), $P = 0.0002$ (*npl* versus *gh9c2*), $P < 0.0001$ (*gh9c2 npl* versus *gh9c2*). *P* value (**d**): $P = 0.0026$ (*gh9c2* versus WT), $P = 0.1162$ (*gh9c1* versus WT), $P = 0.0030$ (*gh9c1 gh9c2* versus WT), $P = 0.0023$ (*npl* versus WT), $P < 0.0001$ (*gh9c2 npl* versus WT), $P < 0.0001$ (*gh9c2 npl* versus *gh9c2*), $P < 0.0001$ (*gh9c2 npl* versus *npl*). N = 12 plants. Scale bars, 1 cm (**a**), 20 μm (**b**).

degradation to secure the transcellular IT progression. It is presently unclear how these cell wall enzymes are secreted to specific locations for either building infection structures or help releasing rhizobia. It was found that the "infectosome" protein complex might mediate polarized exocytosis during IT development and the IT location of NPL was affected in one infectosome mutant, *rpg*[73–77]. A coherent secretory pathway for GH9s needs to be elucidated and whether they will be regulated by the infectosome awaits further study[78]. *GH9Cs* are widely present in plants and our data suggests that *GH9C2* was recruited into the NIN regulon to enable rhizobial colonization during the evolution of nodulation. Although NIN-independent regulation of other *GHs* presumably exists in legumes that become infected via rhizobial "crack entry"[79], we speculate that *GH9C2* homologs may play conserved roles in SYM type nodules[63]. Future studies on *GH9Cs* and other cellulases in different types of root nodule symbioses will help shed light on the molecular and evolutionary mechanisms underlying cell wall remodeling during symbiotic colonization in land plants.

## Methods

### Plant and rhizobia materials

*M. truncatula* ecotypes R108 and Jemalong A17 were used in this study as WT. *gh9c1-1* (NF11668), *gh9c2-1* (NF16578) and *gh9b3-1* (NF5823) were *Tnt1* retrotransposon insertion mutants (R108 background), all of which were identified in this study. *npl-1* (NF18556) is a *Tnt1* insertion mutant in R108 background[49], which was also used to generate *gh9c2-1 npl-1* double mutant in this study. *gh9c1-1 gh9c2-1* was made in this study by crossing *gh9c1-1* and *gh9c2-1*.

*M. truncatula* seeds were treated with sulfuric acid for 10 min, and then were washed 6 times with sterilized $ddH_2O$. After being treated with bleach for 4 min, seeds were washed 6 times again with sterilized $ddH_2O$. Then seeds were imbibed in sterilized $ddH_2O$ over 2 h before being transferred onto water plates (0.4% agar), and then were kept at 4 °C for 2 days. Before sowing, seeds were kept in dark at 22 °C overnight. For symbiotic phenotyping, germinated seedlings were sown in a mixture of vermiculite and perlite (1:1) and grown in controlled environment chambers (24 °C, 16 h light/8 h dark).

Rhizobial strains used in this study were *S. meliloti* strains Rm1021 (Rm1021) harboring pXLGD4 (hemA:lacZ) (*Rm1021-LacZ*) or a pHC60[80] derived plasmid conferring constitutive Cerulean CFP expression (*Rm1021-CFP*), Rm1021 *nifH:GUS*[81] and mCherry tagged *S. meliloti 2011* (Sm2011-mCherry).

### Rhizobial infection and nodulation phenotyping

*M. truncatula* seedlings were inoculated with *S. meliloti 1021-LacZ* (overnight culture at 28 °C, $OD_{600}$ = 0.05) 3 days after growing in vermiculite and perlite (1:1). For rhizobial infection phenotyping, plants were harvested at 7 dpi or 14 dpi. Roots were cut off and fixed in 2.5% glutaraldehyde for 1 h before being stained in 0.8 mg $mL^{-1}$ X-Gal (5-Bromo-4-chloro-3-indolyl-ß D-galactoside, Sangon Biotech, Shanghai, China) solution (100 mM sodium phosphate, 10 mM KCl, 1 mM $MgSO_4$, pH = 7.4) at 28 °C overnight in dark. Rhizobial infection events indicated by blue staining of rhizobia were quantified into different categories, including MCs, elongating infection threads (eIT), fully elongated ITs in root hairs (IT) and ITs ramified beyond epidermis (rIT). Abnormal infections such as enlarged MCs, blocked ITs, etc., of each stages, were quantified as defective/abnormal infection events. For nodulation phenotyping, nodules were harvested at 7, 10, 14 dpi to observe early infection processes in nodules, or at 21, 28 dpi for later phenotypes. For infection phenotyping in nodules, nodules were stained with X-Gal before embedded in 5% agar and sectioned up to 60 µm using a Leica VT1200 vibratome. To obtain higher resolution of rhizobial infection in nodules, after dehydrated through a graded ethanol series, some nodules were embedded in Paraffin (Biosharp, Beijing, China) and were sectioned at a thickness of 5 µm with a Leica RM 2235 rotary microtome before staining with 0.5% toluidine blue for 10 min. Images of infection threads, nodules and nodule sections were captured using a digital camera mounted on a Zeiss Axio Scope. A1 microscope or a Leica DM2500 LED microscope.

### Hairy root transformation mediated by *Agrobacterium rhizogenes*

*Agrobacterium rhizogenes* ARqua1 strain was transformed with binary vectors by electroporation and used to generate composite plants comprising a transgenic hairy root system with non-transformed aboveground parts[82]. To generate transgenic plants used for live cell imaging, after germination, seed coats were removed from cotyledons with a pair of forceps and radicles were cut off about one third from the root tip to create wounding sections for *A. rhizogenes* ARqua1 culture to infect. The seedlings were then placed onto solid Fahräeus medium for 1 week in controlled environment growth chamber. One week later, plants were placed to another fresh solid Fahräeus medium which contain extra 100 mM Augmentin (United Laboratories, China) to avoid *A. rhizogenes* overgrowth for 4 days. Plants were then moved to modified Fåhraeus medium (Fåhraeus minus $NH_4NO_3$, plus 3 mM $MgSO_4$ and 100 nM 2-amino ethoxyvinyl glycine (AVG)) for future rhizobial inoculation. For transgenic plants used for other purposes, seedlings were punctured using a syringe needle to cause 3–4 wounds on radicles while injecting *A. rhizogenes* ARqua1 cultures. After 2–3 weeks growing, transgenic roots were screened and positive plants were kept growing in controlled environment growth chamber for inoculation with rhizobia for further phenotyping or protein localization analysis.

### GUS staining Assay

A 2196 bp *GH9C2* promoter was amplified by using Phanta Max Super-Fidelity DNA Polymerase (Vazyme, Nanjing, China) and cloned into entry vector pDONR207 by using Gateway BP clonase (Invitrogen). The BP products pDONR207-pGH9C2 was then cloned into the destination vector pKGWFS7 using Gateway LR clonase (Invitrogen) to make *pGH9C2:GUS*. The *pGH9B3:GUS* construct was made by Golden Gate cloning[83]. A 2161 bp promoter of *GH9B3* was synthesized by Sangon Biotech (Shanghai, China) and was used as a level 0 module, and then cloned into level 1 vector then level 2 backbone vector EC50507. Transgenic hairy root plants harboring corresponding promoter-GUS vectors were grown for 3 weeks in controlled environment chamber before inoculated with *S.meliloti 1021-LacZ* ($OD_{600}$ = 0.05). Plants were harvested at 7 dpi and 21 dpi respectively and stained with 1 mg $mL^{-1}$ X-Gluc solution (100 mM potassium phosphate, 1 mM potassium ferricyanide, 1 mM potassium ferrocyanide, 10 mM EDTA, pH = 7.0) at 37 °C in dark for several hours to overnight. For observing GUS staining in nodules, 7 dpi and 21 dpi nodules were collected and sectioned with a vibratome.

For nifH-GUS assay, WT and *gh9c2-1* plants were inoculated with S. *meliloti 1021 nifH:GUS*. Nodules were harvested at 14, 21 and 28 dpi for GUS staining and then were sectioned at a thickness of 60 µm. Ratios of numbers of positive GUS-stained nodules to all nodules used for GUS assay at each stage were used as a proxy for rhizobia nitrogenase synthesized in the corresponding genotypes.

### RNA isolation and RNA interference

For RNA isolation, root tissues were harvested and flash-frozen in liquid nitrogen. Total RNA was extracted using the FastPure Universal Plant Total RNA Isolation Kit (Vazyme, China), followed by cDNA synthesis with the HiScript III RT SuperMix for qPCR (+gDNA wiper) according to the manufacturer's protocols.

The 451 bp (*GH9C1*) and 318 bp (*GH9B3*) fragments were amplified from A17 cDNA and cloned into entry vectors pDONR207 or pDONR221. These fragments were subsequently recombined into destination vector pK7GWIWG2 (II) RR[84] via Gateway cloning to produce *GH9C1-RNAi* and *GH9B3-RNAi* vectors, respectively. Empty pK7GWIWG2 (II) RR vector without insert as the control (*EV*). These constructs were introduced into *M. truncatula* via hairy root transformation. Transgenic hairy root plants were inoculated with *S.meliloti 1021-LacZ* and nodulation phenotype was quantified at 21 dpi. Gene expression levels were analyzed by qRT-PCR. Relative expression levels were calculated using $2^{-\Delta Cq}$ method and normalized with *Elongation Factor 1α* (*EF1α*) as the reference gene.

### Live-cell confocal imaging of fluorescent protein fusions

All constructs unless otherwise mentioned were made using Golden Gate cloning. DNA fragments of coding sequences and promoters for *GH9C1, GH9C2* and*GH9B3* were synthesized by Sangon Biotech (Shanghai) except that *GH9C2* promoter was PCR amplified from genomic DNA using Phanta Max Super-Fidelity DNA Polymerase (Vazyme, Nanjing, China). CBM3a was identified from *Clostridium thermocellum*[70]. The DNA sequence was downloaded from NCBI (Gene ID35803981), and a DNA fragment corresponding to Asn368-Pro522 was synthesized. These were used as level 0 modules and level 1 modules were assemble to make *pLjUBQ1:GH9C2-GFP*, *pGH9C2:GH9C2-GFP, pLjUBQ1:GH9C1-GFP, pGH9C1:GH9C1-GFP* and *pLjUBQ1:YPet-CBM3a*. Level 2 vectors with backbone EC50507 were then made by incorporating another level 1 vector *pAtUBQ10:DsRed* as a transgenic marker and control for protein subcellular localization. $GH9C2^{\Delta CBM49}$ fragment was PCR amplified from *GH9C2* DNA fragment. The *GH9C2* C-terminal fragment immediately after CBM49 domain region was designed as primers (Supplementary Data 4) and was added to $GH9C2^{\Delta CBM49}$ by PCR to make sure only CBM49 domain was deleted in $GH9C2^{\Delta CBM49}$. $GH9C2^{\Delta CBM49}$ fragment was designed as a Golden Gate level

0 module and level 2 vectors were made for *pGH9C2:GH9C2$^{\Delta CBM49}$-GFP* and *pLjUBQ1:GH9C2$^{\Delta CBM49}$-GFP* respectively. For subcellular localization of GH9C2 and GH9C2$^{\Delta CBM49}$ in nodules, transgenic hairy roots harboring *pGH9C2:GH9C2-GFP pAtUBQ10:DsRed* or *pGH9C2:GH9C2$^{\Delta CBM49}$-GFP pAtUBQ10:DsRed* construct were generated in both WT and *gh9c2-1* background respectively. For co-localization constructs, *pNPL:NPL-GFP*[49] and *pGH9C2:GH9C2-tdTomato* were used as level 1 vectors for making the level 2 vector *pGH9C2:GH9C2-tdtomato pNPL:NPL-GFP*. A new level 1 vector *pNPL:NPL-tdTomato* was made and used to make *pGH9C2:GH9C2-GFP pNPL:NPL-tdTomato*.

A confocal laser microscopy-based live-cell imaging system for observing rhizobial infection in *M. truncatula* root hairs was used in this study[17]. Transgenic hairy roots harboring different constructs were cultured on plates containing modified Fahraeus medium with 3 mM $MgSO_4$, 0.5% Phytagel and 100 nM 2-aminoethoxyvinyl glycine (AVG,) vertically in a growth room. The roots were covered with Lumox film (Sarstedt, UK) and were inoculated with *S. meliloti 1021-CFP, S. meliloti 1021-lacZ* or *S. meliloti 2011-mCherry* (OD = 0.001). From 3 dpi onwards roots were imaged at different infection stages under a Leica STELLARIS 5 or Olympus FV3000 confocal laser scanning microscope system. For the plasmolysis experiment, transgenic roots harboring a *pLjUBQ1:GH9C2-mCherry* construct were incubated in 300 mM sorbitol solution for about 15 min before root hairs being imaged.

For observing protein localization and subcellular dynamics during rhizobial infection and rhizobial release in nodules, nodules were collected from composite transgenic plants at 7, 10 and 14 dpi. Nodules were then hand sectioned and nodule sections were mounted to slides in PBS buffer for further imaging using a Leica STELLARIS 5 or Olympus FV3000 confocal laser scanning microscope system.

Wavelengths for fluorophores excitation (ex) and signals collections (em) were with the following settings: GFP 488 nm (ex) / 500-530 nm (em); YPet 488 nm (ex) / 520-540 nm (em); DsRed 561 nm (ex) / 570–610 nm (em); mCherry 561 nm (ex) / 600-630 nm (em); tdTomato 561 nm (ex) / 570–610 nm (em) and CFP 457 nm (ex) / 465–485 nm (em). Confocal image analyses and Z-projections (maximal) were performed with Fiji (ImageJ)[85] or FV31S-SW, and the video was exported by Imaris software. GFP and YPet were pseudo colored in green, CFP and mCherry were pseudo colored in magenta, and DsRed, tdTomato were pseudo colored either in red or magenta.

### *gh9c2-1* complementation assay

In all complementation experiments, *pGH9C2:GH9C2-GFP pAtUBQ10:DsRed* was introduced into *gh9c2-1*, and an Empty vector (EV) was introduced into WT R108 and *gh9c2-1*, as positive and negative controls, respectively, by *A. rhizogenes* mediated hairy root transformation. For the complementation experiment testing the functional relevance of in vivo cellulase activities, amino acid residues were chosen for mutation to Ala by searching Uniprot and three residues, i.e., H414, D466 and E475 were selected[58–61]. Then three additional binary vector constructs were introduced into *gh9c2-1*, which were *pGH9C2:GH9C2(H/A)-GFP, pGH9C2:GH9C2(DE/AA)-GFP* or *pGH9C2:GH9C2(HDE/AAA)-GFP* in combination with *pAtUBQ10:DsRed*. These constructs were made using Mut Express II Fast Mutagenesis Kit (Vazyme) based on *pGH9C2:GH9C2-GFP pAtUBQ10:DsRed* construct. For the complementation experiment testing the functional relevance of CBM49 domain for GH9C2 function in rhizobial infection and rhizobial release, three additional constructs, *pGH9C2:GH9C2$^{\Delta CBM49}$-GFP pAtUBQ10:DsRed, pGH9C2:GH9C2.2-GFP pAtUBQ10:DsRed* and *pGH9C2:GH9B3-GFP pAtUBQ10:DsRed* were introduced into *gh9c2-1*. DNA fragment of *GH9C2.2* was amplified by Phanta Max Super-Fidelity DNA Polymerase (Vazyme, Nanjing, China) and was assembled into Golden Gate vector. *pGH9C2:GH9B3-GFP pAtUBQ10:DsRed* was also made by Golden Gate cloning. For complementation of rhizobial infection, transgenic roots were harvested at 14 dpi for quantification of different categories of infection events. Nodules were collected at 14 dpi and double stained with Calcofluor White and SYTO13 for rhizobial colonization analysis using nodule sections imaged under confocal microscopy. Rhizobial colonization ratio in nodules was quantified as the area of SYTO13-stained cells to the area of all nodule cells in ImageJ software: the area of nodule cells was selected by "Freehand" selections tool and designated as S1; from S1 area, colonized nodule cells which were stained with SYTO13 were selected with "Wand" Tool and the area was designated as S2; rhizobial colonization ratio was calculated with following formula: colonization ratio = S2 / S1. Nodules harvested at 28 dpi were also used for complementation assay with pink nodules and white nodules of each genotype of plants quantified. Whole nodule images of bright field or DsRed channels were captured using a Manual Zeiss Axio Zoom.V16 microscope and analyzed with ZEN 3.4 software.

### Protein expression in *Pichia pastoris*

To produce protein of GH9C2 catalytic domain (GH9C2$^{CD}$, comprising amino acids 25-501), the corresponding coding sequence was amplified. The catalytic domain (CD) and carbohydrate binding domain 49 (CBM49) of GH9C2 were identified using HMM library and genome assignments server of Superfamily (https://supfam.org/SUPERFAMILY/index.html). Signal Peptide was predicted using SignalP-6.0 (https://services.healthtech.dtu.dk/services/SignalP-6.0/). The amplified fragment was subsequently cloned into the pPICZαA expression vector between *EcoR*I and *Sal*I restriction sites using the ClonExpress II One Step Cloning Kit (Vazyme, China) to generate C-terminal 6xHis-tagged expression construct *pAOX1:GH9C2$^{CD}$-6xHis*. The recombinant plasmid was linearized by *Pme*I digestion and transformed into *Pichia pastoris* SMD1168 strain via electroporation. The empty pPICZαA vector was transformed into *P. pastrois* as a negative control.

The protein expression was performed as described previously with modification[86]. Briefly, a single zeocin-resistant colony was inoculated into 5 mL YPD medium supplemented with 1 mg $mL^{-1}$ zeocin and incubated at 28 °C with shaking at 220 rpm overnight. Subsequently, 5 mL pre-culture was used to inoculate 50 mL Buffered Glycerol-complex Medium (BMGY; containing 1% yeast extract, 2% peptone, 1.34% YNB, 1% glycerol, 100 mM phosphate buffer at pH = 6.0 and 4 × $10^{-5}$% biotin). Following overnight cultivation at 28 °C with 220 rpm agitation, cells were harvested by centrifugation at 1000 g for 10 min. The pellet was resuspended in 50 mL Buffered Methanol-complex Medium (BMMY; containing 1% yeast extract, 2% peptone, 1.34% YNB, 1% methanol, 100 mM phosphate buffer at pH = 6.0 and 4×$10^{-5}$% biotin) for 24 h protein induction at 28 °C. The culture supernatant was then collected by centrifugation at 10,000 g for 10 min at 4 °C and stored at 4 °C for subsequent protein expression analysis and cellulase activity assay. Protein concentrations were determined using the Bradford Protein Assay Kit (Beyotime Biotechnology, China). A standard curve was generated with bovine serum albumin (BSA) to calculate protein concentrations in the samples.

For western blot, total proteins (5 µL culture supernatant) were separated on 8% (w/v) SDS-PAGE gel at 120 V for 1 h. The separated proteins were transferred to a polyvinylidene difluoride (PVDF) membrane at 300 mA for 1 h. The membrane was washed with Tris-buffered saline containing 0.1% Tween 20 (TBST) and blocked with 5% (w/v) non-fat milk in TBST at room temperature for 90 min. After TBST wash once, PVDF membrane was incubated overnight at 4 °C with anti-His primary antibody (TransGen Biotech, China; 1:5000 dilution in TBST). Following four additional TBST washes, the membrane was incubated with HRP-conjugate anti-mouse IgG secondary antibody (Absin Bioscience, China; 1:10,000 dilution in TBST) for 1 h at room temperature. Protein signals were detected by incubating membrane with SuperSignal™ West Pico PLUS Chemiluminescent Substrate (Thermo Fisher Scientific, USA) for 5 min, followed by image acquisition using a Tanon 4800 Multi multi-functional imaging system.

### Cellulase activity assay

Cellulase activity of recombinant proteins was quantified by measuring reducing sugar released from substrate hydrolysis using the 3,5-dinitrosalicylic acid (DNS) method[57]. To determine optimal pH, 250 μL reaction mixtures containing 3 μg total protein and 0.5% (w/v) carboxymethylcellulose (CMC, M.W. 90000 (DS = 0.7), 50-100 mPa.s) were prepared in the following buffer solutions (50 mM final concentration): sodium citrate (for pH = 3–6), sodium phosphate (for pH = 7) and Tris-HCl (for pH = 8–9) at 37 °C for 1 h[40]. For optimal temperature determination, reactions were conducted under established optimal pH conditions at temperatures ranging from 20 °C to 80 °C.

The substrate specificity of recombinant proteins was assessed by conducting enzymatic reactions under optimized conditions (pH and temperature) for 1 h, using the following polysaccharide substrates at specified concentrations (w/v): 1% microcrystalline cellulose (MCC; Sangon Biotech), 1% CMC (Macklin), 0.5% lichenan (Macklin), 1% arabinan (Macklin), 0.5% glucomannan (Macklin), 1% xylan (Sangon Biotech) or 1% pectin (Sangon Biotech). Following enzymatic reactions, 50 μL of each reaction solution was mixed with 100 μL DNS reagent and incubated at 95 °C for 10 min for developing color. The mixture was rapidly cooled and absorbance at OD = 540 was measured using a Tecan Spark Multimode Microplate Reader. A standard curve was generated using glucose to calculated reducing sugar content. Culture supernatant from empty vector transformants was served as negative control for background subtraction.

### Cell wall extraction

The cell wall extraction was adapted from previously reported methods with modifications[87]. Briefly, roots were harvested at 14 dpi and ground into fine powder in liquid nitrogen with a mortar. The powder was suspended in 20 mL chloroform/methanol (1:1, v/v) and shaken at room temperature for 1 h. The pellet was collected by centrifugation at 5000 g for 10 min, then washed four times with 70% (v/v) ethanol through repeated centrifugation and resuspension to obtain the alcohol-insoluble residue (AIR). After being suspended in 100% acetone and centrifuged at 5000 g for 10 min, the AIR was air-dried in a fume hood at room temperature for 2 days.

### Monosaccharide composition analysis

Monosaccharide composition was analyzed as previously described with modifications[88]. For each measurement, 5 mg of AIR powder was mixed with 1 mL of 2 M trifluoroacetic acid (TFA) and incubated at 121 °C for 2 h. The sample was then blown dry under a nitrogen stream and washed three times with 3 mL methanol. The resulting residue was dissolved in 1 mL of distilled water.

For PMP (1-phenyl-3-methyl-5-pyrazolone) derivatization, the sample solution (0.2 mL) was mixed with 0.2 mL 0.5 M NaOH and 0.5 mL 0.5 M PMP methanolic solution. The mixture was vortexed thoroughly and incubated at 70 °C for 1 h, and neutralized with 0.2 mL 0.5 M HCl. Excess PMP was removed through three extractions with 1 mL chloroform each. After discarding the chloroform layer, 0.3 mL of the solution was transferred and diluted to 1 mL with distilled water.

The diluted solution was filtered through a 0.22 μm membrane filter, and 10 μL of the filtrate was analyzed using a Thermo U3000 high-performance liquid chromatography (HPLC) system equipped with an Agilent ZORBAX Eclipse XDB-C18 column (4.6 × 250 mm, 5 μm). Separation was achieved with a mobile phase of acetonitrile/phosphate buffer (17:83, v/v, pH = 6.8) at 0.8 mL/min flow rate. Monosaccharides were quantified by comparing retention times and peak areas to monosaccharide standards (Man, mannose; GlcN, glucosamine; Rha, rhamnose; GlcA, glucuronic acid; GalA, galacturonic acid; Glc, glucose; Gal, galactose; Xyl, xylose; Ara, arabinose; 0.5 mg $mL^{-1}$ each; Yuanye Bio-Technology, China).

### Cell wall polysaccharide measurement

Cellulose content was measured using the Updegraff method[89]. Briefly, 2 mg of AIR samples were mixed with 0.25 mL 2 M TFA and incubated at 121 °C for 90 min. The pellet was collected by centrifugation at 13,500 g for 10 min at room temperature. The residue was then suspended in 1 mL acetic acid/nitric acid/water (8:1:2, v/v/v) by thorough vortex and incubated at 100 °C for 30 min. After washing three times with acetone, the residue was dried at 45 °C and resuspended in 72% (v/v) sulfuric acid.

To measure Glucose (Glc) concentration, 0.1 mL of the supernatant was mixed with 0.2 mL 2 mg $mL^{-1}$ anthrone for developing color. Reaction was carried out at 80 °C for 30 min, and the absorbance of the sample at OD = 625 was measured using a Multiskan GO multimode reader. Glucose was used as standard for calculation of cellulose content.

For total hemicellulose measurement, 2 mg of AIR sample was also mixed with 0.25 mL 2 M TFA and incubated at 121 °C for 90 min. After centrifugation, 0.15 mL supernatant was transferred to a new centrifuge tube and dried at 60 °C. The residue was then suspended in 0.3 mL methanol and vortexed thoroughly. After dring again at 60 °C, the residue was dissolved in 0.5 mL distilled water. Next, 0.08 mL solution was transferred to a fresh centrifuge tube and mixed with 0.06 mL DNS reagent[57]. The mixture was incubated in boiling water for 10 min, and the absorbance at OD = 540 was measured. Xylose was used as standard for measurement.

To determine the pectin content of cell walls, 5 mg of AIR samples were thoroughly vortexed with 1 mL sulfuric acid. After centrifugation at 13,500 g for 10 min, 0.2 mL supernatant was transferred to a new centrifuge tube and mixed with 0.05 mL carbazole-ethanol solution[90]. The mixture was constantly shaken, followed by the rapid addition of 1 mL concentrated sulfuric acid. After incubation at 85 °C for 20 min, the absorbance at OD = 525 was measured. D-Galacturonic acid (Sigma-Aldrich, USA) was used as the standard.

### Confocal microscopy of nodules with fluorescent dyes

Nodules of different genotypes were harvested at 10 dpi and fixed in 2.5% (v/v) glutaraldehyde at least for 1 h. Before staining, nodules were sectioned at a thickness of 60 μm with a vibratome. For phenotyping of rhizobial release, the sections were double stained with Pontamine Fast Scarlet 4B (S4B) (Macklin, Shanghai, China) and SYTO13 Green-Fluorescent Nucleic Acid Stain (Life Technologies). Sections were firstly stained with S4B at a concentration of 1% (w/v) for 5 min. Then samples were washed for 3-5 times with distilled water. Then the sections were stained with SYTO13 at a concentration of 5 μM for 20 min in dark and washed with distilled water 3 times.

For phenotyping of rhizobial infection in nodule, sections were double stained with Calcofluor White Stain (Sigma Aldrich) and SYTO13. The sections were first stained with SYTO13 as described above and washed for 3 times with distilled water. Then the samples were transferred onto microscope slide with one drop of Calcofluor White solution (consisting of 0.1% (w/v) Calcofluor White M2R and 0.05% (w/v) Evans blue) and one drop of 10% (w/v) KOH for 1 min before imaging.

Wavelengths for fluorophores excitation (ex) and signals collections (em) were with the following settings: SYTO13, 488 nm (ex) / 500-530 nm (em); S4B, 561 nm (ex) / 570-650 nm (em); Calcofluor White 405 nm (ex) / 420-470 nm (em). Images were captured using an Olympus FV3000 confocal laser scanning microscope system. Confocal image analyses were performed with FV31S-SW software. SYTO13 was pseudo colored in green, S4B and Calcofluor White were pseudo colored in magenta.

### Transmission electron microscopy

WT R108 and *gh9c2-1* nodules were harvested at 14 dpi for Transmission Electron Microscropy. The nodules were cut longitudinally and

immediately fixed in 0.1 M PBS buffer containing 2.5% glutaraldehyde and 4% paraformaldehyde at room temperature under vacuum for 3 h and then left at 4 °C overnight. The samples were washed with 0.1 M PBS buffer for 3 times and post-fixed in 1% (w/v) $OsO_4$ overnight at room temperature. After being washed for 3 times, the samples were dehydrated in following ethanol graded series: 30% EtOH, 50% EtOH, 70% EtOH, 95% EtOH at room temperature for 20 min each, twice 100% EtOH for 30 min. Once dehydrated, the nodules were gradually infiltrated with a mixture of SpurrResin (SPI Supplies) and acetone in the following proportions (1:3, 1:1, 3:1), with each infiltration step lasting 24 h. To infiltrate sufficiently, the samples were then incubated with 100% resin for 24 h twice. For polymerization, the samples were placed in a baking oven at 70 °C for two days. Sectioned at a thickness of 70 nm using a Leica EM UC7 ultramicrotome, the sections were collected with 200 mesh copper grids and double stained with 2% uranyl acetate and Reynolds lead citrate solution, each staining lasting for 5 mins. Samples were viewed using a Tecnai T12 120 kV transmission electron microscope with Eagle CCD and CryoBox. Images were exported in tif format and analysed using ImageJ to measure thickness of infection thread cell wall.

### Root hair phenotyping in *gh9c1-1*

For root hair phenotyping, seeds were sown on a layer of filter paper on plates containing modified Fåhraeus medium (Fåhraeus minus $NH_4NO_3$, plus 3 mM MgSO4). For g*h9c1-1* complementation assay, *pGH9C1:GH9C1-GFP pAtUBQ10:DsRed* was introduced into *gh9c1-1*, and an Empty vector (EV) was introduced into R108 and *gh9c1-1*, as positive and negative control, respectively, by *A. rhizogenes* mediated hairy root transformation described as above. Roots were harvested at 4 days post sowing for *gh9c1-1* root hair phenotyping, or harvested at 14 days after transformation for *gh9c1-1* complementation assay. Roots were transferred onto plates with water and images were collected using a Manual Zeiss Axio Zoom.V16 microscope. To measure the length and width of root hairs, images were analyzed with ImageJ. Root hairs were measured segmentally according to different developmental stages, for which 21 or 16 (in the *gh9c1-1* complementation assay) root "segments" were delineated continuously, starting from 1500 µm from the root tip, each with a length of 620 µm.

### Reporting summary

Further information on research design is available in the Nature Portfolio Reporting Summary linked to this article.

## Data availability

The authors declare that all data supporting the findings of this study are available within the article and its Supplementary Data files. Source data are provided with this paper.

## References


1. Sprent, J. I. *Legume Nodulation: A Global Perspective*. (Wiley Blackwell, 2009).
2. Roy, S. et al. Celebrating 20 years of genetic discoveries in legume nodulation and symbiotic nitrogen fixation. *Plant Cell* **32**, 15–41 (2020).
3. Jhu, M. Y. & Oldroyd, G. E. D. Dancing to a different tune, can we switch from chemical to biological nitrogen fixation for sustainable food security?. *PLoS Biol.* **21**, e3001982 (2023).
4. Jiang, S. et al. NIN-like protein transcription factors regulate leghemoglobin genes in legume nodules. *Science* **374**, 625–628 (2021).
5. Venado, R. E. et al. Tissue-specific regulation of lipid polyester synthesis genes controlling oxygen permeation into *Lotus japonicus* nodules. *Proc. Natl Acad. Sci. USA.* **119**, e2206291119 (2022).
6. Oldroyd, G. E., Murray, J. D., Poole, P. S. & Downie, J. A. The rules of engagement in the legume-rhizobial symbiosis. *Annu. Rev. Genet.* **45**, 119–144 (2011).
7. Parniske, M. Uptake of bacteria into living plant cells, the unifying and distinct feature of the nitrogen-fixing root nodule symbiosis. *Curr. Opin. Plant Biol.* **44**, 164–174 (2018).
8. Gage, D. J. Infection and invasion of roots by symbiotic, nitrogen-fixing rhizobia during nodulation of temperate legumes. *Microbiol. Mol. Biol. Rev.* **68**, 280–300 (2004).
9. Murray, J. D. Invasion by invitation: rhizobial infection in legumes. *Mol. Plant Microbe Interact.* **24**, 631–639 (2011).
10. Gao, J. P., Liang, W., Liu, C. W., Xie, F. & Murray, J. D. Unraveling the rhizobial infection thread. *J. Exp. Bot.* **75**, 2235–2245 (2024).
11. de Carvello-Nibel, F., Fournier, J., Becker, A. & Arancibia, M. M. Cellular insights into legume root infection by rhizobia. *Curr. Opin. Plant Biol.* **81**, 102597 (2024).
12. Quilbé, J., Montiel, J., Arrighi, J. F. & Stougaard, J. Molecular mechanisms of intercellular rhizobial infection: novel findings of an ancient process. *Front. Plant Sci.* **13**, 922982 (2022).
13. Liu, C. W. & Murray, J. D. The role of flavonoids in nodulation host-range specificity: an update. *Plants (Basel).* **5**, 33 (2016).
14. Krönauer, C. & Radutoiu, S. Understanding Nod factor signalling paves the way for targeted engineering in legumes and non-legumes. *Curr. Opin. Plant Biol.* **62**, 102026 (2021).
15. Fournier, J. et al. Remodeling of the infection chamber before infection thread formation reveals a two-step mechanism for rhizobial entry into the host legume root hair. *Plant Physiol.* **167**, 1233–1242 (2015).
16. Wang, D., Dong, W., Murray, J. & Wang, E. Innovation and appropriation in mycorrhizal and rhizobial symbioses. *Plant Cell* **34**, 1573–1599 (2022).
17. Fournier, J. et al. Mechanism of infection thread elongation in root hairs of *Medicago truncatula* and dynamic interplay with associated rhizobial colonization. *Plant Physiol.* **148**, 1985–1995 (2008).
18. Brewin, N. J. Plant cell wall remodelling in the Rhizobium legume symbiosis. *Crit. Rev. Plant Sci.* **23**, 293–316 (2004).
19. Ivanov, S. et al. Rhizobium-legume symbiosis shares an exocytotic pathway required for arbuscule formation. *Proc. Natl Acad. Sci. USA* **109**, 8316–8321 (2012).
20. Delmer, D., Dixon, R. A., Keegstra, K. & Mohnen, D. The plant cell wall-dynamic, strong, and adaptable-is a natural shapeshifter. *Plant Cell.* **36**, 1257–1311 (2024).
21. Cosgrove, D. J. Structure and growth of plant cell walls. *Nat. Rev. Mol. Cell Biol.* **25**, 340–358 (2024).
22. Wolf, S. Cell wall signaling in plant development and defense. *Annu. Rev. Plant Biol.* **73**, 323–353 (2022).
23. Anderson, C. T. & Kieber, J. J. Dynamic construction, perception, and remodeling of plant cell walls. *Annu. Rev. Plant. Biol.* **71**, 39–69 (2020).
24. Rui, Y. & Dinneny, J. R. A wall with integrity: surveillance and maintenance of the plant cell wall under stress. *New Phytol.* **225**, 1428–1439 (2020).
25. Bellincampi, D., Cervone, F. & Lionetti, V. Plant cell wall dynamics and wall-related susceptibility in plant-pathogen interactions. *Front Plant Sci.* **5**, 228 (2014).
26. Höfte, H. & Voxeur, A. Plant cell walls. *Curr. Biol.* **27**, R865–R870 (2017).
27. Zhang, B., Gao, Y., Zhang, L. & Zhou, Y. The plant cell wall: biosynthesis, construction, and functions. *J. Integr. Plant Biol.* **63**, 251–272 (2021).
28. Vicré, M. & Lionetti, V. Editorial: Plant cell wall in pathogenesis, parasitism and symbiosis, Volume II. *Front Plant Sci.* **14**, 1230438 (2023).

29. Lionetti, V. & Métraux, J. P. Plant cell wall in pathogenesis, parasitism and symbiosis. *Front Plant Sci.* **5**, 612 (2014).
30. Pedersen, G. B., Blaschek, L., Frandsen, K. E. H., Noack, L. C. & Persson, S. Cellulose synthesis in land plants. *Mol. Plant.* **16**, 206–231 (2023).
31. Hoffmann, N., King, S., Samuels, A. L. & McFarlane, H. E. Subcellular coordination of plant cell wall synthesis. *Dev. Cell.* **56**, 933–948 (2021).
32. Coen, E. & Cosgrove, D. J. The mechanics of plant morphogenesis. *Science* **379**, eade8055 (2023).
33. Dora, S., Terrett, O. M. & Sanchez-Rodriguez, C. Plant–microbe interactions in the apoplast: communication at the plant cell wall. *Plant Cell* **34**, 1532–1550 (2022).
34. van Boerdonk, S., Saake, P., Wanke, A., Neumann, U. & Zuccaro, A. beta-Glucan-binding proteins are key modulators of immunity and symbiosis in mutualistic plant-microbe interactions. *Curr. Opin. Plant Biol.* **81**, 102610 (2024).
35. Munzert, K. S. & Engelsdorf, T. Plant cell wall structure and dynamics in plant-pathogen interactions and pathogen defence. *J. Exp. Bot.* **76**, 228–242 (2025).
36. Plant Cell Walls – Research Milestones and Conceptual Insights, edited by Anja Geitmann. Boca Raton, FL: CRC Press. ISBN: 9781032013213 (hbk), https://doi.org/10.1201/9781003178309 (2024).
37. Lopez-Casado, G., Urbanowicz, B. R., Damasceno, C. M. & Rose, J. K. Plant glycosyl hydrolases and biofuels: a natural marriage. *Curr. Opin. Plant Biol.* **11**, 329–337 (2008).
38. Urbanowicz, B. R. et al. Structural organization and a standardized nomenclature for plant endo-1,4-beta-glucanases (cellulases) of glycosyl hydrolase family 9. *Plant Physiol.* **144**, 1693–1696 (2007a).
39. Urbanowicz, B. R. et al. A tomato endo-beta-1,4-glucanase, SlCel9C1, represents a distinct subclass with a new family of carbohydrate binding modules (CBM49). *J. Biol. Chem.* **282**, 12066–12074 (2007b).
40. Kundu, S. & Sharma, R. Origin, evolution, and divergence of plant class C GH9 endoglucanases. *BMC Evol. Biol.* **18**, 79 (2018).
41. la, L. & Karppinen, K. Characterization of cellulases from softening fruit for enzymatic depolymerization of cellulose. *Carbohydr. Polym.* **343**, 122493 (2024).
42. Edema, H., Bawin, T., Olsen, S., Krause, K. & Karppinen, K. Parasitic dodder expresses an arsenal of secreted cellulases with multisubstrate specificity during host invasion. *Plant Physiol. Biochem.* **210**, 108633 (2024).
43. Rich, M. K., Schorderet, M. & Reinhardt, D. The role of the cell wall compartment in mutualistic symbioses of plants. *Front Plant Sci.* **5**, 238 (2014).
44. Balestrini, R. & Bonfante, P. Cell wall remodeling in mycorrhizal symbiosis: a way towards biotrophism. *Front Plant Sci.* **5**, 237 (2014).
45. Wanke, A. et al. A GH81-type β-glucan-binding protein enhances colonization by mutualistic fungi in barley. *Curr. Biol.* **33**, 5071–5084 (2023).
46. Rae, A. L., Bonfante-Fasolo, P. & Brewin, N. J. Structure and growth of infection threads in the legume symbiosis with Rhizobium leguminosarum. *Plant J.* **2**, 385–395 (1992).
47. Vandenbosch, K. A. et al. Common components of the infection thread matrix and the intercellular space identified by immunocytochemical analysis of pea nodules and uninfected roots. *EMBO J.* **8**, 335–341 (1989).
48. Xie, F. et al. Legume pectate lyase required for root infection by rhizobia. *Proc. Natl Acad. Sci. USA* **109**, 633–638 (2012).
49. Liu, C. W. et al. NIN acts as a network hub controlling a growth module required for rhizobial infection. *Plant Physiol.* **179**, 1704–1722 (2019).
50. Zhang, X. et al. Molecular module GmPTF1a/b-GmNPLa regulates rhizobia infection and nodule formation in soybean. *New Phytol.* **241**, 1813–1828 (2024).
51. Su, C. et al. Transcellular progression of infection threads in *Medicago truncatula* roots is associated with locally confined cell wall modifications. *Curr. Biol.* **33**, 533–542 (2023).
52. Robledo, M. et al. Rhizobium cellulase CelC2 is essential for primary symbiotic infection of legume host roots. *Proc. Natl Acad. Sci. USA* **105**, 7064–7069 (2008).
53. Breakspear, A. et al. The root hair "infectome" of *Medicago truncatula* uncovers changes in cell cycle genes and reveals a requirement for Auxin signaling in rhizobial infection. *Plant Cell* **26**, 4680–4701 (2014).
54. Jardinaud, M. F. et al. A Laser Dissection-RNAseq Analysis Highlights the Activation of Cytokinin Pathways by Nod Factors in the *Medicago truncatula* Root Epidermis. *Plant Physiol.* **171**, 2256–2276 (2016).
55. Liu, Z. et al. Single-nucleus transcriptomes reveal spatiotemporal symbiotic perception and early response in Medicago. *Nat. Plants* **9**, 1734–1748 (2023).
56. Anderson, C. T., Carroll, A., Akhmetova, L. & Somerville, C. Real-time imaging of cellulose reorientation during cell wall expansion in Arabidopsis roots. *Plant Physiol.* **152**, 787–796 (2010).
57. Miller, G. L. Use of dinitrosalicylic acid reagent for determination of reducing sugar. *Anal. Chem.* **31**, 426–428 (1959).
58. The UniProt Consortium UniProt: the universal protein knowledgebase in 2023. *Nucleic Acids Res.* **51**, D523–D531 (2023).
59. Tomme, P. et al. Identification of a histidyl residue in the active center of endoglucanase D from Clostridium thermocellum. *J. Biol. Chem.* **266**, 10313–10318 (1991).
60. Tomme, P., van Beeumen, J. & Claeyssens, M. Modification of catalytically important carboxy residues in endoglucanase D from Clostridium thermocellum. *Biochem. J.* **285**, 319–324 (1992).
61. Guerriero, G. et al. Novel insights from comparative in silico analysis of green *Microalgal Cellulases*. *Int. J. Mol. Sci.* **19**, 0–0 (2018).
62. Downie, J. A. Legume nodulation. *Curr. Biol.* **24**, R184–R190 (2014).
63. Tsyganova, A. V., Brewin, N. J. & Tsyganov, V. E. Structure and development of the legume-rhizobial symbiotic interface in infection threads. *Cells* **29**, 1050 (2021).
64. de Faria, S. M. et al. The innovation of the symbiosome has enhanced the evolutionary stability of nitrogen fixation in legumes. *New Phytol.* **235**, 2365–2377 (2022).
65. Zhang, X., Wu, J., Kong, Z. Cellular basis of legume-rhizobium symbiosis. *Plant Commun*. https://doi.org/10.1016/j.xplc.2024.101045 (2024).
66. Yano, K. et al. CERBERUS, a novel U-box protein containing WD-40 repeats, is required for formation of the infection thread and nodule development in the legume-Rhizobium symbiosis. *Plant J.* **60**, 168–180 (2009).
67. Murray, J. D. et al. Vapyrin, a gene essential for intracellular progression of arbuscular mycorrhizal symbiosis, is also essential for infection by rhizobia in the nodule symbiosis of *Medicago truncatula*. *Plant J.* **65**, 244–252 (2011).
68. Kuppusamy, K. T. et al. LIN, a Medicago truncatula gene required for nodule differentiation and persistence of rhizobial infections. *Plant Physiol.* **136**, 3682–3691 (2004).
69. Guan, D. et al. Rhizobial infection is associated with the development of peripheral vasculature in nodules of *Medicago truncatula*. *Plant Physiol.* **162**, 107–115 (2013).
70. Blake, A. W. et al. Understanding the biological rationale for the diversity of cellulose-directed carbohydrate-binding modules in prokaryotic enzymes. *J. Biol. Chem.* **281**, 29321–29329 (2006).
71. del Campillo, E., Gaddam, S., Mettle-Amuah, D. & Heneks, J. A tale of two tissues: AtGH9C1 is an endo-β-1, 4-glucanase involved in root hair and endosperm development in Arabidopsis. *PLoS ONE* **7**, e49363 (2012).

72. Zhang, G. & Ott, T. Cellular morphodynamics and signaling around the transcellular passage cleft during rhizobial infections of legume roots. *Curr. Opin. Cell Biol.* **91**, 102436 (2024).
73. Lace, B. et al. RPG acts as a central determinant for infectosome formation and cellular polarization during intracellular rhizobial infections. *Elife* **12**, e80741 (2023).
74. Li, X. et al. RPG interacts with E3-ligase CERBERUS to mediate rhizobial infection in *Lotus japonicus*. *PLoS Genet* **19**, e1010621 (2023).
75. Liu, M. et al. CERBERUS is critical for stabilization of VAPYRIN during rhizobial infection in *Lotus japonicus*. *New Phytol.* **229**, 1684–1700 (2021).
76. Liu, C. W. et al. A protein complex required for polar growth of rhizobial infection threads. *Nat. Commun.* **10**, 2848 (2019).
77. Deng, J. L. et al. A deeply conserved amino acid required for VAPYRIN localization and function during legume-rhizobial symbiosis. *New Phytol.* **243**, 14–22 (2024).
78. Gavrin A. et al. VAMP721a and VAMP721d are important for pectin dynamics and release of bacteria in soybean nodules. *New Phytol.* **210**, 1011–1021 (2016).
79. Bhattacharjee, O. et al. Nodule INception-independent epidermal events lead to bacterial entry during nodule development in peanut (*Arachis hypogaea*). *New Phytol.* **236**, 2265–2281 (2022).
80. Cheng, H. P. & Walker, G. C. Succinoglycan is required for initiation and elongation of infection threads during nodulation of alfalfa by Rhizobium meliloti. *J. Bacteriol.* **180**, 5183–5191 (1998).
81. Lang, C., Smith, L. S. & Long, S. R. Characterization of novel plant symbiosis mutants using a new multiple gene-expression reporter Sinorhizobium meliloti strain. *Front. Plant Sci.* **9**, 76 (2018).
82. Boisson-Dernier, A. et al. Agrobacterium rhizogenes-transformed roots of Medicago truncatula for the study of nitrogen-fixing and endomycorrhizal symbiotic associations. *Mol. Plant Microbe Interact.* **14**, 695–700 (2001).
83. Patron, N. J. et al. Standards for plant synthetic biology: a common syntax for exchange of DNA parts. *New Phytol.* **208**, 13–19 (2015).
84. Limpens, E. et al. RNA interference in *Agrobacterium rhizogenes*-transformed roots of Arabidopsis and Medicago truncatula. *J. Exp. Bot.* **55**, 983–992 (2004).
85. Schindelin, J. et al. Fiji: an open-source platform for biological-image analysis. *Nat. methods* **9**, 676–682 (2012).
86. Haeger, W. et al. New players in the interaction between beetle polygalacturonases and plant polygalacturonase-inhibiting proteins: insights from proteomics and gene expression analyses. *Front Plant Sci.* **12**, 660430 (2021).
87. Fry, S. C. et al. *The Growing Plant Cell Wall: Chemical And Metabolic Analysis*. (New York: Longman Scientific & Technical) (1988).
88. De Ruiter, G. A. et al. Carbohydrate analysis of water-soluble uronic acid-containing polysaccharides with high-performance anion-exchange chromatography using methanolysis combined with TFA hydrolysis is superior to four other methods. *Anal. Biochem.* **207**, 176–185 (1992).
89. Updegraff, D. M. Semimicro determination of cellulose in biological materials. *Anal. Biochem.* **32**, 420–424 (1969).
90. Bitter, T. & Muir, H. M. A modified uronic acid carbazole reaction. *Anal. Biochem.* **4**, 330–334 (1962).


## Acknowledgements

We thank Z. Zhao, M. Su, and R. Zhang for help on protein expression, tissue embedding & sectioning and light microscopy systems, Z.-B. Liu for help on confocal microscopy and A.-L. Yin for help on TEM sample preparations. We thank The Samuel Roberts Noble Foundation for the *M. truncatula Tnt1* insertion mutant lines. We thank all members of the C.-W. Liu group for their helpful discussions. This work was supported by CAS Project for Young Scientists in Basic Research (grant no. YSBR-011), National Natural Science Foundation of China (grants no. 32321001, 32470250, 32170249), start-up Funding by University of Science and Technology of China and Chinese Academy of Sciences (KY2070000098, KY9100000057, KJ2070000077) and the Fundamental Research Funds for the Central Universities of China (WK2070000193) to C.-W.L.

## Author contributions

C.-W.L. conceptualized and supervised the project. L.Z. and C.-W.L. designed the experiments. L.Z. and C.-Y.J. performed the experiments. L.Z., C.-Y.J., J.D.M. and C.-W.L. analyzed the data. L.Z., C.-W.L. and J.D.M. wrote the paper with input from C.-Y.J.

## Competing interests

The authors declare no competing interests.

## Additional information

**Supplementary information** The online version contains supplementary material available at https://doi.org/10.1038/s41467-025-62083-4.

**Correspondence** and requests for materials should be addressed to Cheng-Wu Liu.

**Peer review information** *Nature Communications* thanks Clara Sanchez-Rodriguez and the other, anonymous, reviewer(s) for their contribution to the peer review of this work. [A peer review file is available].